Cerebral Cortex, May 2020;30: 3352–3369

doi: 10.1093/cercor/bhz314
Advance Access Publication Date: 10 February 2020
Original Article

ORIGINAL ARTICLE

Local Perturbations of Cortical Excitability Propagate Differentially Through Large-Scale Functional Networks

Zachary P. Rosenthal[1,2,3], Ryan V. Raut[2,4], Ping Yan[3], Deima Koko[3], Andrew W. Kraft[8], Leah Czerniewski[3,6], Benjamin Acland[2,5], Anish Mitra[1,2,4], Lawrence H. Snyder[5,6], Adam Q. Bauer[4,6], Abraham Z. Snyder[3,4], Joseph P. Culver[4,6,7], Marcus E. Raichle[3,4,5,6] and Jin-Moo Lee[3,4,6,†]

[1]Medical Scientist Training Program, Washington University School of Medicine, St. Louis, MO, 63110, USA, [2]Graduate Program of Neuroscience, Washington University School of Medicine, St. Louis, MO, 63110, USA, [3]Department of Neurology, Washington University School of Medicine, St. Louis, MO, 63110, USA, [4]Department of Radiology, Washington University School of Medicine, St. Louis, MO, 63110, USA, [5]Department of Neuroscience, Washington University School of Medicine, St. Louis, MO, 63110, USA, [6]Department of Biomedical Engineering, Washington University School of Medicine, St. Louis, MO, 63110, USA, [7]Department of Physics, Washington University School of Medicine, St. Louis, MO, 63110, USA and [8]Department of Medicine, Brigham and Women's Hospital, Harvard Medical School, Boston, MA, 02115, USA

Address correspondence to Zachary P. Rosenthal, BJCIH 9302, 660 S Euclid Ave, St. Louis, MO, 63110, USA. Email: rosenthalz@wustl.edu; Jin-Moo Lee, Email: leejm@wustl.edu
[†]Lead contact

Abstract

Electrophysiological recordings have established that GABAergic interneurons regulate excitability, plasticity, and computational function within local neural circuits. Importantly, GABAergic inhibition is focally disrupted around sites of brain injury. However, it remains unclear whether focal imbalances in inhibition/excitation lead to widespread changes in brain activity. Here, we test the hypothesis that focal perturbations in excitability disrupt large-scale brain network dynamics. We used viral chemogenetics in mice to reversibly manipulate parvalbumin interneuron (PV-IN) activity levels in whisker barrel somatosensory cortex. We then assessed how this imbalance affects cortical network activity in awake mice using wide-field optical neuroimaging of pyramidal neuron GCaMP dynamics as well as local field potential recordings. We report 1) that local changes in excitability can cause remote, network-wide effects, 2) that these effects propagate differentially through intra- and interhemispheric connections, and 3) that chemogenetic constructs can induce plasticity in cortical excitability and functional connectivity. These findings may help to explain how focal activity changes following injury lead to widespread network dysfunction.

Key words: calcium imaging, excitability, functional connectivity, inhibition, parvalbumin interneuron

Introduction

GABAergic interneurons play a vital role in maintaining excitatory/inhibitory (E/I) balance at multiple spatial scales (Bhatia et al. 2019). Such balance homeostatically stabilizes local circuit activity (Maffei et al. 2006; Barral and Reyes 2016), governs plasticity during developmental critical periods (Hensch 2005), and shapes behavior (Yizhar et al. 2011). However, most studies of E/I balance have examined neural activity with microscale techniques such as electrophysiology and two-photon imaging. These spatially restricted approaches may overlook larger scale effects on widely distributed brain networks. Macrolevel techniques such as fMRI and EEG have revealed that within large-scale functional networks (e.g., motor, visual, default mode), interconnected brain loci exhibit synchronized activity, a phenomenon widely known as functional connectivity (FC) (Fox and Raichle 2007). Computational models predict that E/I balance is a key contributor to the organization of FC networks (Deco et al. 2014). In accordance with this prediction, stroke, focal seizures, and traumatic brain injury (TBI) all disrupt regional E/I balance (Carmichael 2012; Mishra et al. 2014; Farrell et al. 2019) as well as brain-wide FC patterns (Silasi and Murphy 2014; Englot et al. 2016; Caeyenberghs et al. 2017), leading to network dysfunction thought to underlie chronic neurocognitive impairment. However, it remains to be empirically determined whether focal E/I imbalance plays a causal role in disrupting large-scale network activity, independent of injury.

The rodent whisker sensorimotor network is a well-characterized large-scale cortical network in mice, both structurally and functionally, making it an ideal model to examine the effects of focal E/I manipulation on systems-scale dynamics. This network exhibits strong monosynaptic projections and intrahemispheric FC between $S1_W$ and the whisker motor cortex ($M1_W$), as well as strong interhemispheric FC between motor cortices, but weaker connectivity between somatosensory cortices (Ferezou et al. 2007; Sreenivasan et al. 2016; Bauer et al. 2018). Recent work emphasizes a prominent role of inhibitory connectivity, in particular parvalbumin interneurons (PV-INs), in gating dynamics within this circuit (Sachidhanandam et al. 2016; Pala and Petersen 2018). PV-INs are the most prevalent GABAergic cell-type, provide fast feedforward inhibition onto pyramidal neuron soma and, as we will expand upon in the Discussion, are critical for regulating local E/I gain control, making them ideal targets for E/I manipulation.

Here, we used virally delivered DREADDs (Designer Receptors Exclusively Activated by Designer Drugs) to reversibly and focally manipulate activity in PV-INs within the mouse whisker barrel somatosensory cortex ($S1_W$). We sought to determine how this perturbation of local E/I balance influences large-scale cortical dynamics by monitoring cortical activity in awake mice using concurrent wide-field optical neuroimaging (GCaMP calcium dynamics in pyramidal neurons) and oxy-hemoglobin hemodynamics (oxy-Hb optical intrinsic signal), as well as local field potential (LFP) recordings in separate experiments. Our results reveal that perturbations in PV-IN activity in $S1_W$ produce local E/I imbalance that propagates differentially through intra- and interhemispheric connections of the whisker sensorimotor network. These findings may allow insight into how brain networks respond to local changes in activity after injury, as well as how large-scale network dysfunction might be counteracted with targeted neuromodulatory therapy.

Materials and Methods

Animal Models

All procedures described below were approved by the Washington University Animal Studies Committee in compliance with AAALAC guidelines. Mice were raised in standard cages in a double barrier mouse facility with a 12–12-h light/dark cycle and ad libitum access to food and water. All mice used in this study were generated as a cross between the *Thy1-GCaMP6f* strain (JAX 024276) and the *PV-Cre* strain (JAX 017320), both on a C57BL/6 J background. Offspring from this cross express GCaMP6f in pyramidal neurons, and Cre recombinase in parvalbumin-expressing interneurons. Prior to experiments, pups were genotyped by PCR to confirm presence of the *Thy1-GCaMP6f* transgene, using the forward primer 5′-CATCAGTGCAGCAGAGCTTC-3′ and reverse primer 5′-CAGCGTATCCACATAGCGTA-3′. Male and female mice from each litter were sorted into experimental groups using a random number generator in MATLAB, so that each litter and sex had balanced representation in each experimental group. No sex specific differences were identified in group-level analyses. Mice were 5–7 weeks of age at the time of viral injection (weights ranging 15–25 g), and were 13–15 weeks of age at the start of imaging or electrophysiology experiments. Data were acquired and pooled over three independent cohorts of mice, with a total of 53 mice used in this study. Staff performing surgical procedures, neuroimaging experiments, and histology were blinded to experimental group.

Viral Injections

Mice received buprenorphine analgesia (SQ, 0.03 mg/kg) and then were anesthetized with isoflurane (3% induction, 1.5% maintenance). Body temperature was maintained via thermostatic heating pad. Mice were secured in a stereotactic frame and then received 200 µL of 20% mannitol per 30 g bodyweight, to prevent brain swelling during surgery. The scalp was shaved, sterilized with isopropyl alcohol and betadine scrub, locally anesthetized with lidocaine, and then incised at midline and retracted. A 0.5-mm burr-hole was drilled out at coordinates for the left whisker barrel cortex from the Paxinos atlas (−1.5 mm posterior, −3.0 mm left of bregma), with intermittent application of chilled saline to the skull. Virus was loaded into a minimally invasive pulled glass pipette (tip OD 20 µm, 40° bevel). To achieve transduction of PV-INs in all cortical layers, virus was delivered in three 100-nL injections (1 nL/s, Nanoject III, Drummond Scientific, Broomhall PA), spaced at 300, 600, and 900 nm depths, pausing for 5 min between injections. Post hoc histology confirmed focal targeting to $S1_W$ (Fig. 1), with no virus expression found in the rest of the cortex. The scalp was then sutured closed and the mice recovered from anesthesia in a heated incubator. Mice were used in experiments 8 weeks later, in order to facilitate strong viral transduction and complete healing of the burr hole and injection tract prior to windowing and wide-field imaging.

Chemogenetic Constructs

All chemogenetic viral vectors were prepared by the Washington University School of Medicine Hope Center Viral Vectors Core: AAV8-hSyn-DIO-hM4D (Gi)-mCherry, AAV8-hSyn-DIO-hM3D (Gq)-mCherry, AAV8-hSyn-DIO-mCherry (titers adjusted to

$\sim 7\times10^{12}$ vg/mL). hM3Dq and hM4Di DREADDs consist of G-protein coupled receptors derived from the M3 or M4 muscarinic acetylcholine channels, mutated by directed evolution such that they are activated by clozapine-N-oxide (CNO) and not by endogenous ligands, leading to net depolarization or hyperpolarization of the resting membrane potential respectively for several hours (Roth 2016). OFF recordings were collected in the absence of CNO, while ON recordings were conducted after intraperitoneal injection of CNO (1 mg/kg, AKSci). This system thus allows for two layers of comparison—between groups (↑/↓PV DREADD versus mCherry-only Control), and within group between OFF and ON states.

Histology Preparation

Mice were deeply anesthetized with FatalPlus (Vortech Pharmaceuticals) and transcardially perfused with heparinized PBS. The brains were removed and fixed in 4% paraformaldehyde for 24 h and transferred to 30% sucrose in PBS. After brains were saturated, they were snap-frozen on dry ice and coronally sectioned (50 µm) on a sliding microtome. Sections were stored in 0.2 M PBS, 30% sucrose, and 30% ethylene glycol at −20°C. GCaMP fluorescence was confirmed in each individual using epifluorescence microscopy (Nikon Eclipse 80i, Nikon Instruments Inc.). As described below, mCherry spatial targeting was subsequently confirmed using DAB immunohistochemistry, while colocalization with parvalbumin was confirmed using fluorescence IHC.

DAB Immunohistochemistry

Sections were rinsed with PBS and then permeabilized with 0.3% PBS-T for 10 min. Sections were then treated with 0.3% H_2O_2 solution in PBS for 10 min to quench endogenous peroxidase activity. Tissue was washed with PBS and blocked with 3% dry milk in PBS-T for 60 min at 25°C. Sections were incubated overnight at 4°C in 1% dry milk in PBS-T solution containing polyclonal rabbit anti-mCherry antibody (1:500, NBP2–25157 Novus Biologicals, Centennial, CO). Sections were washed with PBS, and then incubated for 1 h in blocking solution containing biotinylated antirabbit IgG antibody (1:400, Vector Laboratories). All sections were then incubated with avidin biotinylated enzyme complex (ABC) (1:400, Vector Laboratories) for 1 h. Signal was visualized with 0.025% 3,3′diaminobenzidine (DAB) tetrachloride, 0.25% NiCl, and 0.003% H_2O_2 in 0.05 M tris-HCl (pH 7.6) for 5–15 min. The sections were dried overnight on glass slides, dehydrated, and coverslipped using Permount Mounting Medium (Fisher Scientific) and then viewed with bright-field microscopy. Spatial spread of transduction was manually quantified in ImageJ (NIH) in 5–7 slices per mouse, measuring the medial–lateral width (in mm) and cross-sectional area (in mm^2). DAB staining labels axons and dendritic arbors with better contrast than intrinsic mCherry fluorescence, allowing us to more accurately estimate the spatial extent of DREADD expression. Statistical significance was computed using a one-way ANOVA with Tukey's multiple comparison test, with significance set at an adjusted P-value $< \alpha = 0.05$.

Fluorescence Immunohistochemistry

Sections were pretreated with PBS-T and blocked with 3% dry milk in PBS-T for 1 h at 25°C. Sections were incubated overnight at 4°C in 1% dry milk in PBS-T solution containing polyclonal rabbit antiparvalbumin antibody (1:1000, ab11427, Abcam). After three PBS washes, sections were incubated for 1 h at 37°C in Cy5 AffiniPure Goat Anti-Rabbit IgG (H + L) (1:800; Jackson ImmunoResearch). Sections were washed, mounted, and coverslipped with VECTASHIELD Antifade Mounting Medium with DAPI (Vector Laboratories).

Fluorescence Microscopy and Cell Counting

mCherry and anti-PV fluorescence were examined on an inverted confocal microscope using a 20× objective (Nikon A1-Rsi). The colocalization of mCherry fluorescence and PV-immunoreactive cells was quantified with Imaris colocalization software (Bitplane), using six sections per mouse, three images per section, and centered on the mCherry-labeled injection site. Statistical significance was computed using a one-way ANOVA with Tukey's multiple comparison test, with significance set at an adjusted P-value $< \alpha = 0.05$.

Cranial Windowing

Mice received buprenorphine analgesia (SQ, 0.03 mg/kg) and were anesthetized with isoflurane (3% induction, 1.5% maintenance). Body temperature was maintained via thermostatic heating pad. Mice were secured in a stereotactic frame. The scalp was shaved, sterilized with isopropyl alcohol and betadine scrub, locally anesthetized with lidocaine, and then incised at midline and retracted. A custom Plexiglas window with pretapped screw holes for head fixation was attached to the skull using dental cement (C&B-Metabond, Parkell Inc.), completely containing the surgical opening. Mice were then placed in an incubator to rouse from anesthesia, and were allowed at least 1 week to recover from surgery before experimentation. Windows facilitate head fixation and serial noninvasive imaging in awake animals (Silasi et al. 2016; Wright et al. 2017; Kraft et al. 2018; Mitra et al. 2018). Mice promptly resume normal behavior in their home cages (whisking, grooming, eating) and do not exhibit any signs of pain or distress from their windows.

Surgical Preparation for Electrophysiology

Mice received dexamethasone (20 µL 4 mg/mL, S.C.) 4 h prior to surgery, and 20% mannitol (200 µL/30 g bodyweight, I.P.) immediately prior to surgery. Body temperature was maintained via thermostatic heating pad. Mice were anesthetized using isoflurane anesthesia (3% induction, 1.5% maintenance) and then secured in a stereotactic frame. The scalp was shaved, sterilized with isopropyl alcohol and betadine scrub, locally anesthetized with lidocaine, and then incised at midline and retracted. A circular craniectomy (1 mm in diameter) was drilled out centered over the same left barrel cortex stereotactic coordinates used for viral injection, cooling the brain intermittently with chilled saline. A second (0.5 mm) burr hole was drilled at midline over the cerebellum (3 mm posterior to lambda), and a tungsten ground wire was secured in place using light-cure dental cement. A custom Plexiglas head fixation plate was attached to the skull using C&B-Metabond, completely containing the surgical opening and cerebellar ground electrode. The exposed dura in the barrel cortex craniectomy was protected with an optically clear self-healing polymer gel that allows microelectrode probes to pass into the brain (Dow DOWSIL 3–4680, Ellsworth). Mice were given buprenorphine (SQ, 0.03 mg/kg) at the end of the

procedure for analgesia, and then were given 1 week of recovery time prior to recordings.

Optical Imaging System

Wide-field imaging of cortical calcium dynamics and hemodynamics was performed as previously described (Wright et al. 2017). Sequential illumination was provided by four LEDs: 470 nm (measured peak $\lambda = 454$ nm, LCS-0470-15-22, Mightex Systems), 530 nm (measured peak $\lambda = 523$ nm, LCS-0530-15-22), 590 nm (measured peak $\lambda = 595$ nm, LCS-0590-10-22), and 625 nm (measured peak $\lambda = 640$ nm, LCS-0625-03-22). The 454 nm LED was used for GCaMP excitation, and the 523, 595, and 640 nm LEDs were used for multispectral oximetric imaging. The 523-nm LED was also used as an emission reference for GCaMP6 fluorescence in order to remove any confound of hemodynamics in the fluorescence signal, described below. Both the 454 nm and 523 nm LED light paths were made collinear by using a multiwavelength beam combiner dichroic mirror (LCS-BC25–0505, Mightex Systems). For image detection, we used a cooled, frame-transfer EMCCD camera (iXon 897, Andor Technologies) in combination with an 85 mm f/1.4 camera lens (Rokinon). The acquisition frame rate was 16.8 Hz per channel, with an overall frame rate of ~67 Hz. This frame rate is well above the temporal resolution necessary to characterize GCaMP6 dynamics. To maintain a high frame rate and increase SNR, the CCD was binned at 4 × 4 pixels; this reduced the resolution of the output images from full-frame 512 × 512 pixels to 128 × 128 pixels. Both the LEDs and the exposure of the CCD were synchronized and triggered via a DAQ (PCI-6733, National Instruments) using MATLAB (MathWorks). The field-of-view was adjusted to be approximately 1 cm^2. The resulting pixels were approximately 78 × 78 μm. To minimize specular reflection from the skull, we used a series of linear polarizers in front of the LED sources and the CCD lens. Head-fixed mice were placed at the focal plane of the camera. The combined, collimated LED unit was placed approximately 8 cm from the mouse skull, with a working distance of approximately 14 cm as determined by the acquisition lens. A 515-nm long-pass filter (Semrock) was placed in front of the CCD to filter out 470-nm fluorescence excitation light and a 460/60 nm band-pass filter (Semrock) was used in front of the excitation source to further minimize leakage of fluorescence excitation light through the 515 nm long-pass filter. The pulse durations for the LEDs were 20, 5, 3, and 1 ms for 454, 523, 595, and 640 nm, respectively.

Optical Imaging Recordings

All imaging sessions were performed in awake, unanesthetized mice. Mice were acclimated to head-fixation while secured in comfortable black felt hammock until they resumed normal resting behavior (whisking, grooming, relaxed posture). Mice habituated in this manner are qualitatively observed to be still and relaxed during recordings, and show robust individual FC patterns that we have observed to be highly consistent over consecutive days of repeat recordings. Resting state imaging was collected in 10-min epochs for each mouse at baseline and at 10-min intervals after delivery of CNO (IP injection, 1 mg/kg, AKSci), leaving the mouse fixed in place to preserve an identical field of view between conditions and time points. Whisker stimulation recordings were performed in a separate session, using 5-min epochs per condition (right vs. left side, pre- and post-CNO). Stimulus was delivered using computer-triggered 40 PSI air puffs (Picospritzer, Parker Hannifin, Cleveland, OH) in a block design (5 s rest; 5 s of 1 Hz, 0.1 s puffs; 10 s rest; 15 blocks/5 min total).

Electrophysiology Recordings

All electrophysiology recordings were performed in awake, unanesthetized mice. As in the imaging experiments, mice were acclimated to head-fixation in a black felt hammock until they resumed normal resting behavior. A 1.5 mm 16-channel linear array electrode (NeuroNexus, A1x16-5 mm-100-703-A16, Ann Arbor) was attached with a custom adaptor to a micromanipulator (David Kopf Instruments). The electrode was stereotactically inserted into the brain through the transparent self-healing silicone polymer overlying the dura, enabling direct visualization via surgical stereoscope (Olympus). The probe was inserted to a consistent depth of 1.5 mm using the stereotactic manipulator, with secondary confirmation by 1) visually guiding the most superficial contact to just under the cortical surface, and 2) observing the noise to signal transition as the most superficial electrode moved from noise/air into brain parenchyma. LFPs were recorded using an amplifier with a high-pass filter cutoff of 0.02 Hz (Intan RDH2132) connected to the recording computer through an acquisition board (OpenEphys), with a tungsten reference wire positioned in the cerebellum. All recordings were made inside of a Faraday cage in a completely dark room. For each mouse, baseline recordings were collected in 10-min epochs, followed by CNO injection (IP injection, 1 mg/kg), followed by a 40-min continuous recording, without moving the mouse or the electrode in the brain between baseline and CNO recordings.

Optical Imaging Signal Processing

A binary brain mask was manually drawn in MATLAB for each recording session in each mouse. All subsequent analyses were performed on pixels labeled as brain. Image sequences from each mouse (as well as the brain mask for each mouse) were affine-transformed to Paxinos atlas space using the positions of bregma and lambda (Franklin and Paxinos 2012). A representative frame of baseline light levels in a dark environment, calculated from a mean of dark images collected over 1 min, was subtracted from the raw data. All pixel time traces were then spatially and temporally detrended to correct for any variations in light levels due to photobleaching, LED current drift, and nonuniformity across the skull (Kubota et al. 2008). Reflectance changes in the 523-, 595-, and 640-nm LED channels were used in combination to provide hemoglobin oximetric data using the modified Beer-Lambert Law, as described previously (White et al. 2011). The GCaMP6 fluorescence signal ($\Delta F'$) was corrected for varying concentrations of absorptive hemoglobin using 523-nm LED reflectance, adapting a previously described method.(Ma et al. 2016) Images in each contrast were smoothed with a Gaussian filter (5 × 5 pixel box with a 1.3-pixel standard deviation). Global signal from within the mask-defined brain space was regressed from all data to highlight the underlying subarchitecture of regional connectivity, as done in fMRI preprocessing algorithms.(Fox et al. 2009) Parallel analysis without global signal regression revealed similar correlation changes but with decreased spatial specificity (data not shown). Each imaging session was analyzed for light level fluctuations to identify any epochs exhibiting motion artifact (typically due to displacement of the felt blanket used to tuck mice into their hammock). We subsequently excluded three 5-min epochs of stimulation data

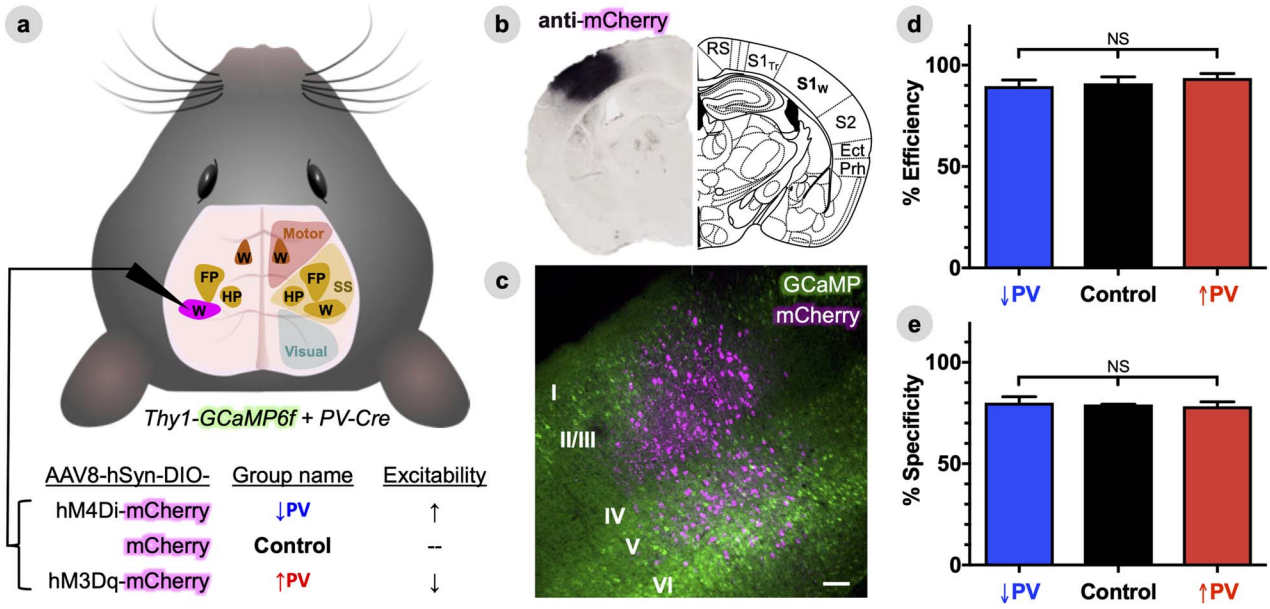

Figure 1. Efficient and specific viral delivery of DREADDs to $S1_W$ parvalbumin interneurons. (*A*), Experimental schematic depicting the brain field of view for wide-field fluorescence imaging, with empirically determined functional territories for whisker (W) FP and hindpaw (HP) plotted within motor and somatosensory (SS) areas (see Methods for ROI determination). Mice were a cross between the *Thy1-GCaMP6f* line, to permit imaging of calcium dynamics in cortical pyramidal neurons, and the *PV-Cre* line, to permit targeting of floxed (DIO) viral constructs to PV-INs. PV-INs in the left whisker barrel primary somatosensory cortex ($S1_W$, magenta) were transduced with one of three different AAV8 vectors for each of the three experimental groups. (*B*), Representative DAB staining of an antibody against the mCherry tag used in AAV8 constructs (left), illustrating focal and well-circumscribed viral transduction of $S1_W$ compared to predicted anatomy from the Paxinos atlas (right). RS = retrosplenial cortex, $S1_{TR}$ = trunk primary S1, S2 = secondary somatosensory cortex, Ect = entorhinal cortex, Prh = perirhinal cortex. (*C*), Representative confocal projection image merging mCherry fluorescence (magenta) in putative PV-INs in $S1_W$ with a background of GCaMP6f fluorescence (green) in pyramidal neurons. Scale bar, 100 µm. (*D*), Average efficiency of viral transduction, calculated within individual mice as the percentage of all PV-immunoreactive cells that also co-labels with mCherry. (*E*), Average specificity of viral transduction, calculated within individual mice as the percentage of all mCherry-labeled cells that also immunostains for PV. Data are represented as mean ± SEM for each group (n = five animals per group), with significance calculated by one-way ANOVA with Tukey's multiple comparison test.

(out of 900 min total across all mice) and two 10-min epochs of resting state data (out of 1380 min total).

Electrophysiology Signal Processing

The 16-channel recordings were referenced to a tungsten ground wire positioned on the cerebellum. To further verify which channels were within the somatosensory cortex, we analyzed the spectral content of all channels, and found similar power in channels 1–12 and then lower power in channels 13–16, indicating that channels 1–12 were in the cortex while channels 13–16 were in subcortical white matter (hence, excluded from analysis). Signal in each channel was decimated (fourth order Chebyshev filter) and then band-pass filtered to 0.01–100 Hz (second order Butterworth filter) to extract LFP. LFP oscillations in each of the 12 cortical channels were observed to be qualitatively similar, and were averaged within each individual mouse to improve SNR. After manually reviewing individual mouse LFP traces for nonstationarities due to suspected motion, 2.5 min of data (in two epochs) were excluded (out of 800 min total).

Optical Imaging ROIs

$S1_W$, $S1_{FP}$, and $M1_W$ regions of interest (ROIs) are based on functional stimulus mapping from an independent cohort of 21 12-week-old *Thy1-GCaMP6f* mice. Whisker stimulation evoked maps were measured in awake mice using air puffs as described above, 5 min/mouse. Forepaw (FP) maps were elicited with mild electrical shocks under anesthesia (86.9 mg/kg of ketamine, 13.4 mg/kg of xylazine, IP) with a heating pad to maintain body temperature. Transcutaneous electrical stimulation of the FP was applied with microvascular clips (Roboz) in a block design (5 s rest; 10 s 3 Hz, 1.0 mA, 0.3 ms electrical pulses; 10 s rest; 15 blocks/5 min total per mouse). About, 15 × 20-s stimulus blocks were averaged within each mouse and then the peak frames for each of 5 air puffs/20-s block or 30 shocks/20-s block were averaged into one mean maximal amplitude frame per mouse. Mean maximal amplitude frames were averaged across mice, and then an evoked response ROI was defined by any pixels whose mean maximal amplitude during stimulus was within > 75% of the maximum pixel intensity within the brain. ROIs generated from this approach are depicted in Figure 1A and were used in subsequent analyses for averaging within functional territories. ROI locations were co-registered to experimental data using affine-transformation to Paxinos atlas space as described in the "Optical imaging signal processing" section above.

Computation of Power Spectral Density

Power spectra for oxy-Hb, GCaMP (Fig. S1A,B) were computed using the fast Fourier Transform (FFT) while power spectra for LFP (Fig. S1C) were computed by averaging all windows of a short time Fourier transform (STFT). Spectra were computed over a 10-min OFF epoch and a 10-min ON epoch beginning 30 min after CNO injection. Spectra were averaged between

mice and then smoothed with a fourth-order Savitzky–Golay filter. Power spectra for LFP in Figure S1D were re-computed using the continuous wavelet transform function in MATLAB (Morse wavelet), and then averaging scalograms across time. Band-limited power differences were quantified for both Fourier and wavelet methods in Figure S2 and statistically verified by two-way ANOVA with Sidak's multiple comparison test, with significance set at an adjusted P-value $< \alpha = 0.05$. In addition, power change (in decibels) was computed using the equation:

$$\Delta Power = 10\log_{10}\left(\frac{Power_{ON}}{Power_{OFF}}\right) \quad (1)$$

Within each mouse, power changes for optical imaging signals (oxy-Hb and GCaMP) were computed by FFT on a pixel-wise basis (shown as maps in Figs 3A and S3), which subsequently averaged within a given ROI (Figs 3C–E and S1E). Power changes for LFP in Figure 3 were computed with the short-time Fourier transform over continuous time series, using the spectrogram function in MATLAB (Hamming window of 6000 samples, 75% overlap), comparing power in each window in the 40-min ON epoch to the time-averaged STFT of the 10-min OFF epoch using equation (1). Statistical significance for power changes (Fig. 3C–F) was computed using a two-way ANOVA with Tukey's multiple comparison test, with significance set at an adjusted P-value $< \alpha = 0.05$. In subsequent analyses of optical imaging data, we focus on the classic BOLD infraslow band (<0.1 Hz) and the delta band (1–4 Hz). These bounds on the delta band were chosen to improve signal to noise, by avoiding a 0.1–1 Hz transition point in global wave propagation that we have previously reported (Mitra et al. 2018), as well as cardiorespiratory peaks at > 5 Hz (observable in Fig. S1).

Computation of Correlation (FC)

For all analyses, FC was computed over specific frequency bands by applying zero-phase filtering (fifth-order Butterworth) directly to GCaMP6 and hemoglobin signals, using 0.02–0.1 Hz for infraslow and 1–4 Hz for the delta band as described above. Pearson correlation, r, was computed in two ways. In order to broadly survey FC changes, we computed correlation matrices in Figure S5 by comparing the time series between every pair of pixels in the brain space, $x_1(t)$ and $x_2(t)$. Thus,

$$r_{x_1x_2} = \frac{1}{\sigma_{x_1}\sigma_{x_2}}\frac{1}{T}\int x_1(t)\cdot x_2(t)dt \quad (2)$$

where σ_{x_1} and σ_{x_2} are the temporal standard deviations of signals x_1 and x_2, and T is the interval of integration. We noted that FC changes were most prominent in the sensory and motor cortices. To enhance signal-to-noise and better visualize these changes, we re-computed correlation maps comparing the average time series within empirically determined whisker S1 and M1 ROIs versus the time series of every pixel in the brain space (Fig. S7). FC for all figures is reported following Fisher z-transformation:

$$z(r) = \tanh^{-1}(r) \quad (3)$$

Pixel-wise FC matrices shown in Figure S5 were sorted into large functional territories using a previously described parcellation (Kraft et al. 2017). Difference matrices (Fig. S5) and maps (Fig. 4 for GCaMP, S6 for oxy-hemoglobin) were computed by array subtraction of FC matrices/maps for a 10-min OFF epoch and a 10-min ON epoch beginning 30 min after CNO injection. Group averaged and individual mouse FC patterns were qualitatively observed to be robust to varying size and shape of seed ROIs centered on $S1_W$ and $M1_W$. Spatial principal component analysis (PCA) was performed on difference matrices by singular value decomposition in MATLAB, generating a topographic map of the first PC weighted by its eigenvalue. Statistical significance for average differences in FC (Fig. 4E–G) between seeds and other ROIs was computed using a two-way ANOVA with Tukey's multiple comparison test, with significance set at an adjusted P-value $< \alpha = 0.05$.

Computation of Event-Triggered Averaging

Event-triggered averaging was used to describe cortical dynamics during local peaks in $S1_W$ GCaMP time-series. For each mouse session, GCaMP time series were averaged within $S1_W$ ROI pixels and then filtered into the delta band (1–4 Hz, fifth-order Butterworth). All local maxima in the delta band were sorted by amplitude; those exceeding the 90th percentile were averaged together within individual mouse sessions (shown in Fig. 5). Differences in group-level averages were statistically verified by two-way ANOVA with Tukey's multiple comparison test, with significance set at an adjusted P-value $< \alpha = 0.05$. In order to determine the impact of paroxysmal bursts on delta-band FC (Fig. S9), five frames preceding and succeeding ($\pm \sim .3$ s) each peak were excised from the time series prior to re-computing ROI seed-based FC as described above. The threshold for removing peaks was varied from the 90th (as above) to the 50th percentile value of all local delta peaks in order to assess FC as a function of increasingly stringent exclusion criteria (i.e., how local activity at different scales contributes to long-range correlations). FC changes following removal of peaks below the 50th percentile value remained stable and are not shown. Differences in FC were statistically verified by two-way ANOVA with Sidak's multiple comparison test, with significance set at an adjusted P-value $< \alpha = 0.05$.

Computation of Whisker-Evoked Sensory Maps

Mean 20-s stimulus blocks were averaged within each mouse and then across mice. Mean response maps shown in Figure 6A,B depict peak frames averaged across 5 air puffs/block. Mean time series in Figure 6A,B were generated by averaging the GCaMP signal for all pixels within right and left $S1_W$ ROIs. GCaMP fluorescence intensity during stimulation was monitored over a 12-h period. Differences between ROIs and groups were verified in Figure 6C,E using a two-way ANOVA with Tukey's multiple comparison test, significance set at an adjusted P-value $< \alpha = 0.05$. Changes over time were statistically verified in Figure 6D using a two-way ANOVA with Dunnett's multiple comparison test, significance set at an adjusted P-value $< \alpha = 0.05$.

Data Presentation and Statistical Analysis

Histograms and scatter plots are presented as group mean ± standard error of the group mean for all experiments, with data points representing individual mice within each group. Color-map data are plotted using the open source Viridis family of color-maps, which are perceptually uniform and robust to colorblindness. Sample sizes were estimated based on prior GCaMP imaging experiments performed by our group.

Randomization and blinding were performed as described above in Animal Models. Prism 8 software was used to perform statistical testing. Statistical significance was computed via one-way ANOVA for histology data in Figure 1, and two-way ANOVA for all other figures. Tukey's multiple comparison test was used for Figures 1, 3, 4–6C,E, S3 and S6; Sidak's test was used in Figures S2 and S9; Dunnett's test was used in Figure 6D. Statistical significance for all figures is reported as not significant ($^{NS}P > 0.05$) or significant ($^{*}P < 0.05$, $^{**}P < 0.01$, $^{***}P < 0.001$, and $^{****}P < 0.001$). Data were verified to be normally distributed prior to statistical testing using the Shapiro–Wilk normality test. Multiple comparison testing was done at the level of individual figure panel plots, including all possible comparisons within each plot within and between groups and ON-OFF states. For the sake of visual clarity, only ON-OFF differences within group are depicted within figures, while significant between-group effects are described in the main text.

Results

Efficient and Specific Viral Delivery of DREADDs to $S1_W$ Parvalbumin Interneurons

We crossed the *Thy1-GCaMP6f* strain of mice (which permit fluorescence neuroimaging of pyramidal neuron calcium dynamics through the intact skull (Wright et al. 2017) with the *PV-Cre* strain (to enable PV-specific expression of floxed viral constructs). Offspring were divided into three groups, each receiving stereotactic injection in the left whisker barrel primary somatosensory cortex ($S1_W$) with a Cre-inducible chemogenetic viral construct: 1) hM3Dq, to increase PV (↑PV) inhibitory activity and decrease excitability, 2) hM4Di, to decrease PV (↓PV) inhibition and increase excitability, or 3) mCherry only, as a Control (Fig. 1A). hM3Dq and hM4Di are Designer Receptors Exclusively Activated by Designer Drugs (DREADDs), engineered muscarinic channels that are activated by the synthetic drug, CNO. The effects of DREADDs on activity in PV-INs have been extensively characterized in prior studies (Kuhlman et al. 2013; Sun et al. 2016; Funk et al. 2017; Liu et al. 2017; Calin et al. 2018; Chandrasekar et al. 2018; Stedehouder et al. 2018; Williams and Holtmaat 2019).

We histologically validated the delivery of DREADD constructs in each group ($n = 5$ mice/group), and found that expression of viral constructs was well-circumscribed within the Paxinos atlas boundaries of $S1_W$ (Fig. 1B), with no detectable expression in the rest of the cortex. Gross spread of viral transduction was similar between groups in both medial-lateral width (control: 1.52 ± 0.16 mm, ↑PV: 1.91 ± 0.15 mm, ↓PV: 1.77 ± 0.09, corrected $^{NS}P = 0.28$), and mean coronal cross-sectional area (Control: 1.33 ± 0.27 mm^2, ↑PV: 1.92 ± 0.26 mm^2, ↓PV: 1.56 ± 0.12 mm^2, $^{NS}P = 0.27$). In addition, mCherry fluorescence in putative PV-INs was distributed in all cortical layers, and did not colocalize with *Thy1*-GCaMP fluorescence in pyramidal neurons (Fig. 1C). Lastly, we compared colocalization of mCherry fluorescence versus immunostaining with an antiparvalbumin antibody. All three virus groups exhibited high transduction efficiency of PV-INs on average, computed within individual mice as the fraction of all PV-immunostaining cells that expresses mCherry (Fig. 1D, Control: $91.0 \pm 3.2\%$, ↑PV: $93.7 \pm 2.2\%$, ↓PV: $89.7 \pm 3.0\%$, corrected $^{NS}P = 0.55$), as well as high specificity, computed as the fraction of all mCherry-expressing cells that immunostains for PV (Fig. 1E, Control: $79.2 \pm 0.2\%$, ↑PV: $78.4 \pm 2.2\%$, ↓PV: $80.1 \pm 2.9\%$, corrected $^{NS}P = 0.88$).

Mice were allowed 8 weeks of recovery after viral injection, after which cranial windows were installed over the skull for wide-field neuroimaging in one set of mice, while $S1_W$ craniotomy ports were installed for LFP recordings in a separate cohort. Mice were then habituated to handling and head-fixation. All subsequent brain recordings were performed in awake animals.

Activating S1W PV-DREADDs Induces Local Changes in Activity and Excitability

To test whether chemogenetic modulation of PV-INs alters local activity, we measured calcium dynamics (GCaMP $\Delta F'$) averaged within $S1_W$ versus LFP recordings averaged over all cortical layers. GCaMP imaging was performed in one cohort with chronic cranial windows over the intact skull (↑PV $n = 12$, ↓PV $n = 12$, Control $n = 11$), while LFP recordings were performed in a separate cohort with an open-skull head fixation (↑PV $n = 5$, ↓PV $n = 6$, Control $n = 5$). GCaMP fluorescence is strongly correlated with multiunit activity (Ma et al. 2016; Murphy et al. 2018). Thus, GCaMP and LFP offer complementary perspectives on both supra- and subthreshold neural ensemble dynamics. Representative time-series from individual mice for both signals are shown in Figure 2A,B at baseline (OFF, black), and 30 min after IP injection of 1 mg/kg CNO (ON, magenta). This time window for recording was chosen on the basis of DREADD effects peaking between 30–60 min after CNO delivery (discussed later in Fig. 6D). No qualitative ON-OFF differences were observed in LFP or GCaMP time-series for either Control or ↑PV mice. However, in the ↓PV group, $S1_W$ disinhibition manifested as paroxysmal hyperexcitability, superimposed on lower amplitude fluctuations. Bursts of hyperexcitability were observed as high amplitude up-peaks in GCaMP fluorescence (Fig. 2A), or down-peaks in LFP (2B).

To assess the spectral frequency content of activity changes, we generated group-averaged power spectra over 10-min-long ON and OFF epochs (shown for GCaMP, LFP, and oxy-Hb in Fig. S1A–D), and then calculated the ON-OFF power change in decibels using equation (1) (S1E). DREADD activation in the ↓PV group broadly increased $S1_W$ spectral power in hemoglobin, GCaMP, and LFP signals. ↑PV and Control mice showed no apparent change. To quantify the distribution of band-limited power changes, we compared the short time Fourier transform (Figs S1C and S2A) and Morse continuous wavelet transform methods for power analysis of full-band LFP data (S1D, S2B). The Fourier method offers improved frequency resolution, while the wavelet method provides stronger temporal resolution and is better suited for the analysis of paroxysmal, nonstationary time series. Both methods demonstrated qualitatively similar results; the Fourier transform was used for computing power spectral density in subsequent analyses. Power increases in the ↓PV group were observed in all frequency bands, achieving significance for activity < 25 Hz (S2A). No significant ON-OFF changes were observed in any band for ↑PV or control mice.

Locally Disrupted $S1_W$ E/I Balance Bidirectionally Modulates Spectral Power Locally and in Remote Sensorimotor Areas

We next explored the spatial extent and temporal evolution of activity changes over a 40-min period after CNO delivery. To measure spatial extent, we scored the mean ON-OFF power change in decibels (delta band, 1–4 Hz, GCaMP) for each pixel

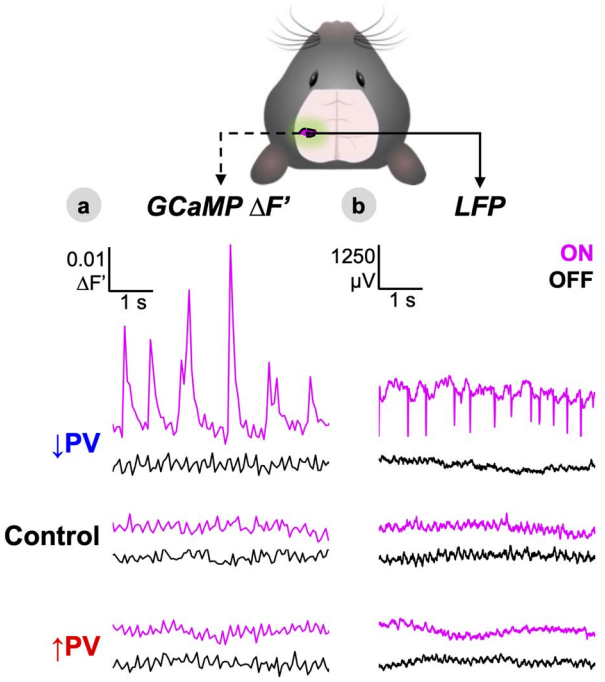

Figure 2. Activating $S1_W$ PV-DREADDs induces local changes in activity and excitability. (*A*,*B*) Representative time-series of GCaMP fluorescence (ΔF′) within the left $S1_W$ ROI (***A***) and separately recorded LFP within $S1_W$ averaged over all cortical layers (*B*) shown for each of the three experimental groups at baseline (OFF, black) and 30 min after delivery of CNO (ON, magenta). See Figures S1 and S2 for quantification of power spectral changes.

in the cortex over successive 10-min windows (Fig. 3*A*). To further characterize temporal evolution over a broader frequency range, we computed group-averaged spectrograms of the 40-min rolling change in 0.02–100 Hz $S1_W$ LFP power (Fig. 3*B*, shown in time-averaged cross-section in S1C,*E*). For comparison with blood oxygen level-dependent (BOLD) functional MRI, we also computed the corresponding infraslow band (0.02–0.1 Hz) power change for the oxy-HB optical intrinsic signal (Fig. S3). GCaMP fluorescence has been shown to offer improved signal-to-noise and spatial specificity compared to the optical intrinsic signal (Murphy et al. 2018), though the two signals are strongly coupled to one another with a temporal offset attributable to neurovascular coupling (Vazquez et al. 2014; Ma et al. 2016; Wright et al. 2017). ON-OFF changes at 30 min post-CNO were statistically verified by two-way ANOVA with Tukey's multiple comparison test, comparing spatially averaged spectral power within functional ROIs (Fig. 3*C–E*; see Methods for ROI definitions) as well as average full-band LFP power (3*F*).

In ↓PV-ON mice (Fig. 3*A*,*B*), bursting events were associated with gradually increased delta band GCaMP power over a large swath of cortex encompassing $S1_W$ (averaging 3.1 mm in medial-lateral width, top row Fig. 3*A*). In addition, a small increase in delta power was observed in the left whisker motor cortex ($M1_W$), a region functionally and structurally connected to $S1_W$. While this remote increase did not achieve significance compared to ↓PV-OFF ($^{NS}P = 0.31$), it was significant compared to Control-ON ($^{*}P = 0.01$). Importantly, these changes are qualitatively mirrored in the infraslow oxy-Hb signal. While we did not observe paroxysmal hyperexcitability in oxy-Hb dynamics as in the GCaMP signal (Fig. S3*A*), we did observe a significant increase in infraslow oxy-Hb power in left $S1_W$ ($^{*}P = 0.001$), but no other within- or between-group changes were statistically significant in any ROI (Fig. S3*B–F*). Lastly, LFP recordings corroborated that spectral power increases ensue within min after CNO injection in ↓PV mice and plateau at 20–30 min. In addition to band limited changes shown in (S2*A*), full-band LFP spectral power in $S1_W$ was significantly increased on average (Fig. 3*F*, $^{****}P < 0.0001$).

Conversely, we anticipated that DREADDs in the ↑PV group would decrease local $S1_W$ power. While a slight local decrease in 1–4 Hz activity was observed (Fig. S1), it was not statistically significant in GCaMP ($^{NS}P = 0.14$, Fig. 3*C*), full-band LFP ($^{NS}P = 0.99$, 3*E*), or band-limited LFP ($^{NS}P = 0.99$, **S2**). Unexpectedly, significant ON-OFF GCaMP power reductions were even more prominent in remote connected regions: ipsilateral/left $M1_W$ ($^{****}P < 0.0001$) as well as contralateral/right $M1_W$ ($^{****}P < 0.0001$) (Fig. 3*A*, quantified in 3*C–E*). No significant infraslow hemodynamic power changes were detected in left or right $S1_W$ or $M1_W$ (Fig. S3).

In addition, we were surprised to discover that, in every ↑PV mouse, motor cortex activity was elevated at baseline in the OFF-state, before the mice had ever been exposed to CNO. ↑PV-OFF mice exhibited elevated delta power in both left $M1_W$ ($^{****}P < 0.0001$) and right $M1_W$ ($^{****}P < 0.0001$) compared to littermates in Control-OFF or ↓PV-OFF. This pattern was consistent across data pooled over two independent cohorts of ↑PV mice. Curiously, we found that OFF-state GCaMP time-series from individual ↑PV mice exhibited paroxysmal hyperexcitability in the motor cortex (Fig. S4), similar to that observed in $S1_W$ in the disinhibited ↓PV-ON mice in Figure 2. No baseline differences between ↑PV-OFF and Control-OFF were found in the area of viral transduction, left $S1_W$, for either GCaMP ($^{NS}P = 0.27$) or full-band LFP ($^{NS}P = 0.99$) power. Importantly, Control mice were transduced with an analogous viral construct that expresses the mCherry tag alone, and no DREADD channel. Control mice exhibited no change in power after administration of CNO, as demonstrated in both GCaMP and LFP in Figures 2 and 3. These baseline differences in motor activity, while unplanned, provide valuable information about how local E/I changes propagate through functional networks. In Figures 4–6, we focus on relative changes in each group from the OFF to ON state (e.g., the acute effect of enhanced inhibition, for the ↑PV group), while also noting informative consequences of the ↑PV group's baseline motor cortex hyperexcitability. The emergence of these baseline differences in CNO-naïve mice over 8 weeks after viral injection as confirmed in a separate cohort in Figure S8 Mechanistic origins of these unexpected findings are considered in the Discussion.

Propagation of Local E/I Imbalance Disrupts Patterns of Cortical Resting-State Functional Connectivity

In order to characterize how these focal changes in excitability spread within cortical networks, we performed two complementary analyses of resting state neuroimaging data: first, mapping the zero-lag correlation structure (functional connectivity, FC) of cortical dynamics across whole time-series, and second, assessing effective connectivity by computing event-triggered average (ETA) responses to high amplitude events in $S1_W$. For stationary, normally distributed activity, these two approaches converge on typical correlation patterns for mouse connectivity: strong homotopic connectivity between left and right cortices (Wright et al. 2017). However, these approaches offer complementary perspectives in the setting of paroxysmal bursting events in the ↑PV-OFF and ↓PV-ON conditions.

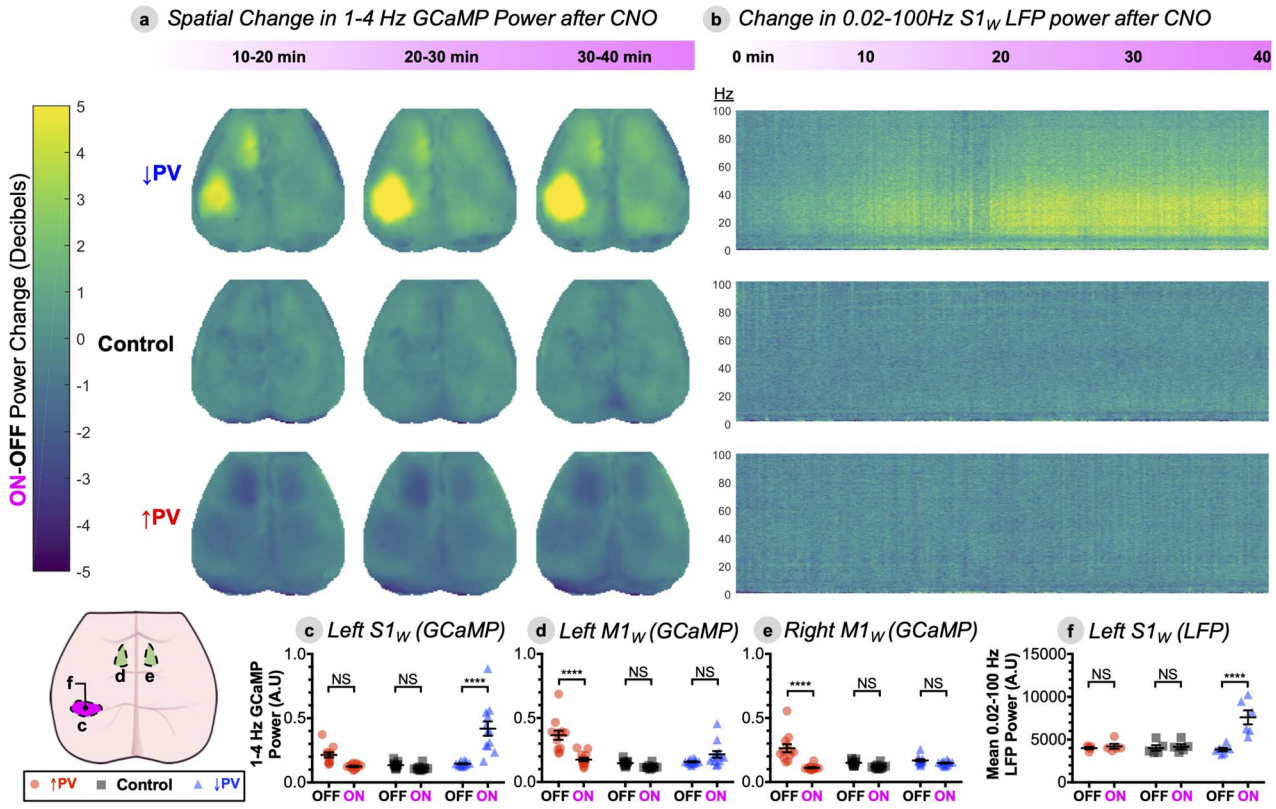

Figure 3. Locally disrupted $S1_W$ E/I balance bidirectionally modulates spectral power locally and in remote sensorimotor areas. (*A*), Change in power spectral density (ΔPower, in decibels) for 1–4 Hz (delta band) GCaMP activity for each pixel in the brain space for each experimental group, comparing three successive 10-min imaging windows after CNO delivery (ON) to a preceding 10-min baseline OFF epoch using equation (1). Data represent group averages (↑PV $n = 12$, ↓PV $n = 12$, Control $n = 11$), quantified within three different ROIs below in *C*–*E*. (*B*), ΔPower spectrogram in $S1_W$ LFP, on same decibel scale as *A*, with frequency on the *y*-axis (Hz) and time (in minutes) on the *x*-axis. ΔPower is computed over a continuous 40-min ON epoch after CNO injection, compared to a preceding 10-min OFF epoch. Data represent group averages (↑PV $n = 5$, ↓PV $n = 6$, Control $n = 5$), quantified in *F*. (*C*–*F*) Statistical verification of trends in three ROIs from the GCaMP data—left $S1_W$ (*C*), left $M1_W$ (*D*), and right $M1_W$ (*E*)—as well as LFP data from left $S1_W$ (*F*). Power spectral density is shown in arbitrary units (A.U.). Individual data points represent individual mice, black bars designate mean ± SEM. Significance was calculated by two-way ANOVA with Tukey's multiple comparison test for each figure panel, comparing both within and between groups. ON-OFF statistical comparisons within group are depicted within each panel, while comparisons between groups are reported in the main text. ($^*P < 0.05$, $^{**}P < 0.01$, $^{***}P < 0.001$, and $^{****}P < 0.0001$). See also Figure S3 for ΔPower maps for infraslow (0.02–0.1 Hz) GCaMP and oxy-Hb.

In order to identify regions undergoing FC changes, we first computed the Fisher z-transformed Pearson correlation, z(r), between time-series of every pair of pixels in the cortex and constructed group-averaged FC matrices in the ON and OFF conditions; ON-OFF ΔFC matrices were computed by subtraction (Fig. S5A). OFF-state FC matrices for Control and ↓PV mice were qualitatively similar, while ↑PV mice exhibited baseline differences from the other two groups, with foci of altered connectivity particularly in S1 and M1 cortices. ON-OFF ΔFC matrices demonstrated no change in Control mice, while ↓PV and ↑PV mice exhibited ON-OFF connectivity changes primarily in somatosensory and motor regions. The localization of FC changes to this network of regions was verified by principal component analysis (Fig. S5B) performed on ΔFC matrices: ~80% of the variance for both ↓PV and ↑PV ON-OFF ΔFC matrices was captured by the first component, which prominently features $S1_W$ and $M1_W$. In contrast, the first component of ON-OFF ΔFC matrices in Control mice explained less than 40% of the variance and did not have a distinctive topography. To visualize FC changes from the perspective of seed regions within the whisker sensorimotor network, we computed FC maps, comparing each pixel's time-series to the average time-series within empirically derived seed ROIs (see Methods) for whisker sensory and motor cortices (Fig. S7). We then computed ON-OFF ΔFC maps for GCaMP by subtraction of data in Figure S7 (Fig. 4A–*D*) and statistically verified key FC changes (Fig. 4E–*G*) by two-way ANOVA with Tukey's multiple comparison test, focusing on homotopic (interhemispheric) FC for $S1_W$ and $M1_W$, as well as intrahemispheric $S1_W$:$M1_W$ sensorimotor FC. To facilitate comparison with BOLD FC data, we conducted parallel FC analyses of the infraslow oxy-Hb optical intrinsic signal (ON-OFF ΔFC maps in Fig. S6 mirror Fig. 4, original ON and OFF maps shown in Fig. S7).

At baseline, ↑PV-OFF mice exhibited heightened three-node synchrony between left $S1_W$ and right/left $M1_W$ (Fig. S7A,C,D). Specifically, ↑PV-OFF mice had stronger baseline intrahemispheric $S1_W$:$M1_W$ correlation than littermates in other groups ($^{****}P < 0.0001$ vs. ↓PV-OFF or Control-OFF, Fig. 4F), as well as stronger $M1_W$ homotopic synchrony ($^{****}P < 0.0001$ vs. either group, Fig. 4G). These differences reversed upon chemogenetic activation of $S1_W$ PV-INs (Fig. 4A,C,D): we observed significant ON-OFF reductions in $S1_W$:$M1_W$ correlation ($^{**}P < 0.0014$) down to Control levels ($^{NS}P = 0.17$ vs. Control-ON, 4F). Likewise, ON-state motor homotopic FC was significantly reduced (ON-OFF $^*P = 0.02$, 4G), though still elevated compared to Control-ON $M1_W$ homotopic FC ($^{***}P < 0.0002$). Interestingly, while baseline

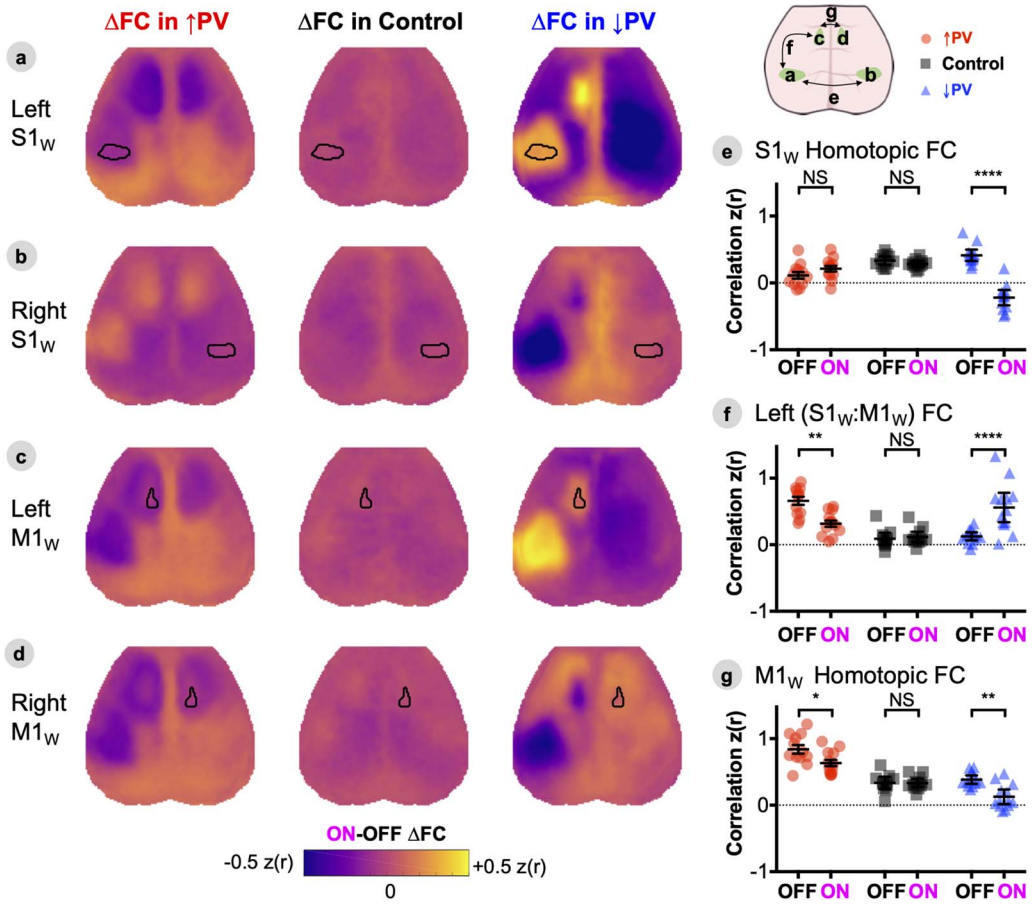

Figure 4. Propagation of local E/I imbalance disrupts patterns of cortical resting-state functional connectivity. *A–D*, ON-OFF ΔFC maps computed by array subtraction of ON and OFF maps shown in Figure S7, for seeds placed in left $S1_W$ (*A*), right $S1_W$ (*B*), left $M1_W$ (*C*), and right $M1_W$ (*D*). Maps are represented as group averages (↑PV $n = 12$, ↓PV $n = 12$, Control $n = 11$). (*E–G*), Statistical verification of changes in homotopic $S1_W$ connectivity (*E*), left $S1_W$:$M1_W$ sensorimotor connectivity (*F*), and homotopic $M1_W$ connectivity (*G*). Individual data points represent individual mice, black bars designate mean ± SEM, with significance calculated by two-way ANOVA with Tukey's multiple comparison test ($^*P < 0.05$, $^{**}P < 0.01$, $^{***}P < 0.001$, and $^{****}P < 0.0001$). See also companion Supplemental Figures S5–7.

hyperexcitability propagated to left and right motor cortices, it was not transmitted interhemispherically from $S1_W$ (Fig. 4E), the area of viral transduction. Indeed, we observed lower baseline ↑PV-OFF $S1_W$ homotopic connectivity ($^{**}P < 0.006$ vs. control-OFF, $^{****}P < 0.0001$ vs. ↓PV-OFF). Activating DREADDs normalized these differences, increasing ↑PV-ON $S1_W$ homotopic FC to Control levels ($^{NS}P = 0.82$ vs. Control-ON). Indeed, baseline hyperconnectivity between left $S1_W$ and right/left $M1_W$ came at the expense of weakened connectivity with all of the rest of the cortex, forming conspicuous regions of negative correlation for seeds placed outside of these three nodes (e.g., weakened OFF-state FC with right $S1_W$, Fig. S7B). Activating $S1_W$ PV-INs reversed these baseline differences. Thus, seeds in these three regions exhibited qualitatively increased FC with the rest of the cortex (orange on ΔFC maps, Fig. 4).

To confirm that differences in ↑PV mice were caused by expression of chemogenetic constructs injected into $S1_W$ 8 weeks prior, we injected DREADDs in a new cohort (↑PV $n = 5$, ↓PV $n = 6$, Control $n = 6$) and installed cranial windows immediately afterwards so that we could monitor FC during the 8-week recovery period after viral injection (Fig. S8). Mice were naïve to CNO throughout this experiment. All three groups exhibited similar patterns of connectivity at week 0 (immediately after injection) that were consistently maintained over 4 weeks of imaging. However, the ↑PV mice diverged after week 6, exhibiting weaker whisker homotopic FC and stronger intrahemispheric $S1_W$:$M1_W$ connectivity. FC changes were concurrent with the emergence of high amplitude bursting activity in $M1_W$ of ↑PV mice (example in Fig. S4), visible as a rightward-shift in histograms of GCaMP intensity in $M1_W$ beginning at week 6 (Fig. S8*D*). Owing to limited sample size, this experiment was not sufficiently powered to match the statistically significant baseline FC differences shown with $n = 12$ beyond the 8-week time point in Figure 4F,G.

↓PV-OFF mice did not exhibit baseline FC differences and were indistinguishable from Control-OFF mice on $S1_W$ homotopic FC ($^{NS}P = 0.74$), $M1_W$ homotopic FC ($^{NS}P = 0.97$) and $S1_W$:$M1_W$ FC ($^{NS}P = 0.998$). However, chemogenetic inhibition of PV-INs dramatically increased $S1_W$:$M1_W$ FC (ON-OFF $^{****}P < 0.0001$) while simultaneously weakening $S1_W$ homotopic FC (ON-OFF $^{****}P < 0.0001$) and $M1_W$ homotopic FC (ON-OFF $^{**}P = 0.0013$).

Control mice did not exhibit any significant changes in FC after delivery of CNO (ΔFC matrices in Fig. S5 and ΔFC maps in Fig. 4). In addition, effects in delta-band GCaMP FC (Fig. 4) for all three groups were qualitatively mirrored in oxy-Hb FC (Fig. S6). We have previously shown that connectivity of the hemoglobin optical intrinsic signal exhibits strong

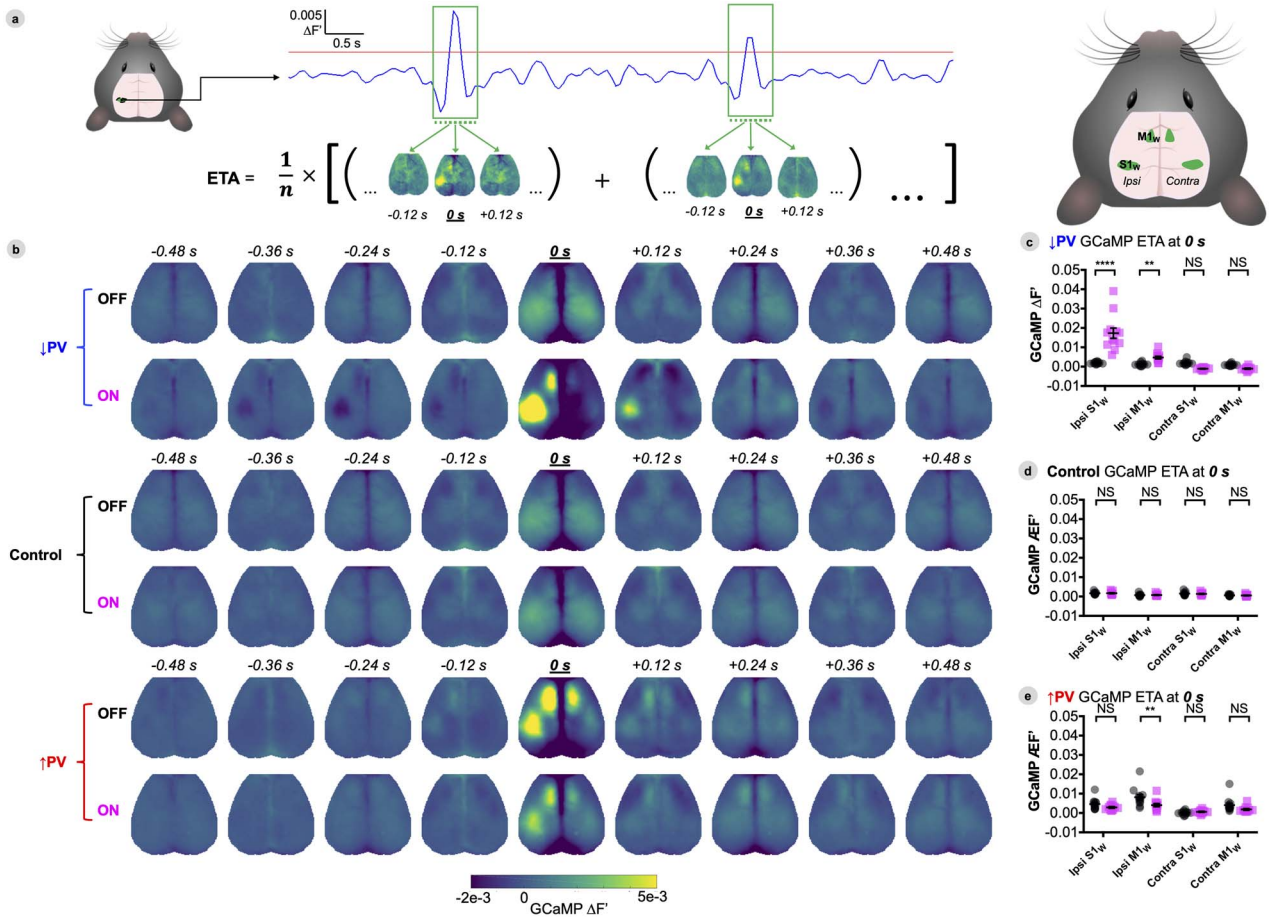

Figure 5. ON-OFF Changes in $S1_W$ ETA activity spread intrahemispherically to $M1_W$ but not to the contralateral hemisphere. (*A*) Illustration of ETA computation. Frames surrounding local peaks above a given threshold (depicted as red line) in the 1–4 Hz GCaMP time series taken from the $S1_W$ region were flagged for averaging (run-specific, percentile-based thresholds were computed as described in Methods). Cortex-wide maps corresponding to the flagged frames were averaged to generate a movie of cortical dynamics preceding and succeeding high-amplitude bursts in $S1_W$. (*B*) Group-averaged GCaMP dynamics surrounding the top 10% of local up-peaks in $S1_W$ (centered at 0 s), with DREADDs ON or OFF. (*C–E*) Average GCaMP fluorescence ($\Delta F'$) within four different ROIs at $t = 0$ s during $S1_W$ peaks for each group. Individual data points represent individual mice, black bars designate mean ± SEM, with significance calculated by two-way ANOVA with Tukey's multiple comparison test (*$P < 0.05$, **$P < 0.01$, ***$P < 0.001$, and ****$P < 0.0001$). Data are shown at baseline (OFF, black) and 30 min after delivery of CNO (ON, magenta). See also Figure S9 to see amplitude distribution of peaks and how they impact FC.

spatial similarity to GCaMP FC (Wright et al. 2017). Indeed hemoglobin FC changes in Figure S6 exhibit similar topography to delta band GCaMP maps, although with more spatial noise (and weakened statistical strength), as expected for infraslow hemodynamics.

ON-OFF Changes in $S1_W$ ETA Activity Spread Intrahemispherically to $M1_W$ but not to the Contralateral Hemisphere

In order to disambiguate how the additive signal of hyperexcitability bursts impacts functional connectivity (Duff et al. 2018), we examined effective connectivity at the event level. All local maxima in $S1_W$ GCaMP time-series for each individual mouse were sorted by amplitude (Fig. S9). ETAs (as shown in Fig. 5A) were computed within mouse by averaging local maxima (thresholded at >90th percentile peaks) at baseline (OFF) and 30 min after delivery of CNO (ON). Group averaged cortical dynamics surrounding $S1_W$ maxima are shown for each condition in Figure 5B (as maps) and S9A (as average time series) with $S1_W$ peaks centered at 0 s. Differences in regional GCaMP peak amplitudes, centered on $S1_W$ peaks, were statistically compared between ipsi- and contralateral $S1_W$ and $M1_W$ within group in Figure 5C–E, with significance determined by two-way ANOVA with Tukey's multiple comparison test. To determine whether the additive signal of high amplitude $S1_W$ activity explains FC changes (Fig. S9C), we compared time series correlation values with all $S1_W$ peaks included (100%), and after removing peaks (and surrounding time points) above a progressively decreasing percentile value before re-computing correlation.

ETA in Control mice revealed that local maxima in $S1_W$ occur synchronously with activation of contralateral $S1_W$ and bilateral motor cortices (with no difference between ON and OFF states, Fig. 5B,D), consistent with the normal correlation structure of the barrel cortex (Fig. S7A,B). The distribution of amplitudes of local maxima in the ON and OFF state were very similar (Fig. S9B). Removing high amplitude peaks from the time series did not introduce ON-OFF correlation differences (Fig. S9C).

As in Control mice, ↓PV-OFF mice exhibited bilaterally symmetric cortical activation patterns surrounding $S1_W$ maxima (Fig. 5C). However, in the ON state, local peaks in $S1_W$ were

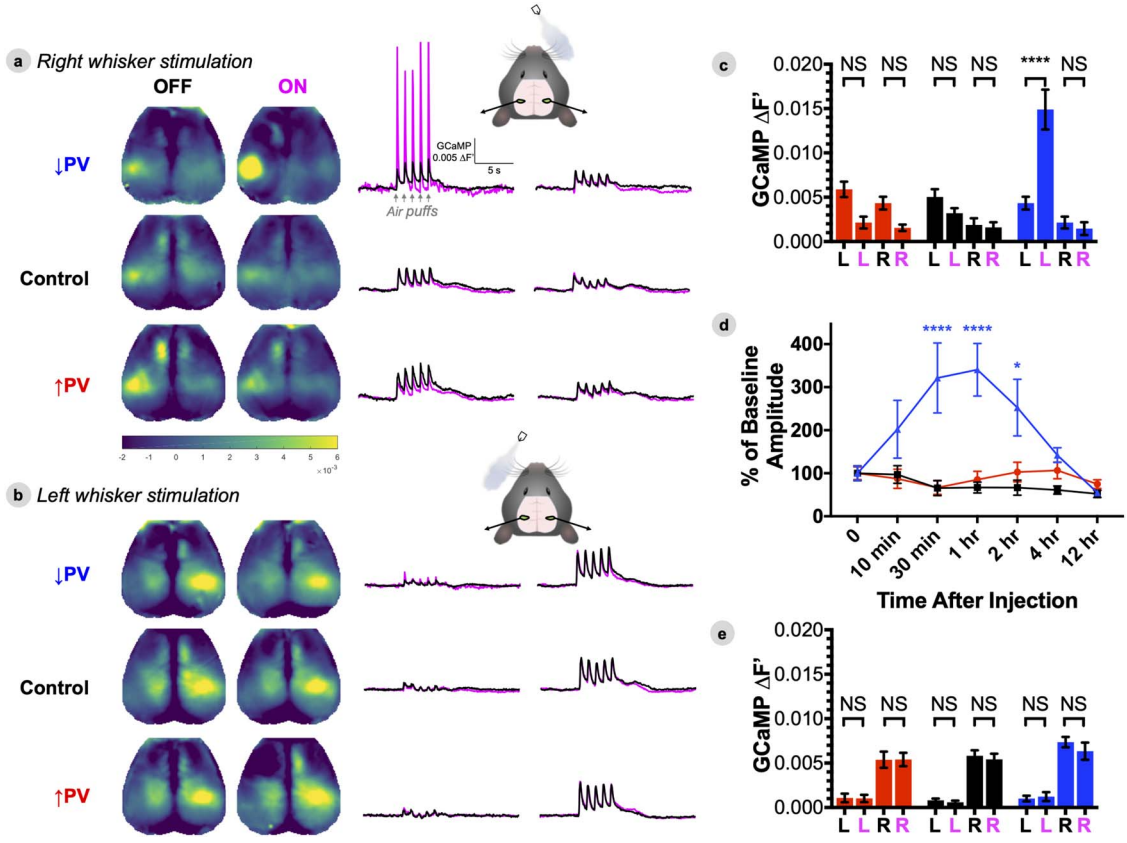

Figure 6. PV-INs modulate $S1_W$ excitability to ascending contralateral sensory inputs, but not ipsilateral inputs. (*A–B*) Group averaged evoked responses to stimulation of the right whiskers (*A*) and left whiskers (*B*) (↑PV $n = 6$, ↓PV $n = 6$, Control $n = 5$). Responses are presented as maps of peak GCaMP fluorescence ($\Delta F'$) during stimulation, and average stimulation block time series for left and right $S1_W$ ROIs. (*C,E*) Average GCaMP fluorescence within left (*L*) and right (*R*) $S1_W$ ROIs during right (*C*) and left (*E*) whisker stimulation, with data represented as mean ± SEM, and comparisons by two-way ANOVA with Tukey's multiple comparison test. (*D*) Time course of CNO effect on right whisker stimulation evoked response, normalized against baseline amplitude, with comparison by two-way ANOVA with Dunnett's multiple comparison test. Data are shown at baseline (OFF, black) and 30 min after delivery of CNO (ON, magenta).

significantly higher in amplitude (****$P < 0.0001$ vs. ↓PV-OFF, Figs 5B,C and S9A), reflecting the high amplitude bursts seen in Figure 2. Closer examination of the distribution of $S1_W$ peaks in Figure S9B demonstrates that nearly all ON maxima were higher in amplitude than OFF maxima. ON-OFF changes in $S1_W$ simultaneously increased ipsilateral $M1_W$ activation (**$P = 0.010$, 5C) while nonsignificantly reducing contralateral activity in $S1_W$ ($^{NS}P = 0.14$) and $M1_W$ ($^{NS}P = 0.63$). This unilateral high amplitude activity directly caused ON-OFF differences in motor homotopic and sensorimotor correlation (Fig. S9C), with differences returning to nonsignificant levels after the top deciles of peak activity were removed from time series. Whisker homotopic FC, however, remained significantly different between ON and OFF at all scales of activity, even after excising time points associated with the top 90% amplitude local peaks from time series (data not shown). We also note that high amplitude bursts in $S1_W$ were, on average, temporally flanked by local decreases in $S1_W$ activity (Figs 5B and S9A).

In ↑PV mice, ETA highlighted important baseline (OFF) differences (Figs 5B,E and S9A): local peaks in left $S1_W$ were significantly higher in amplitude than those on the right side (**$P < 0.0022$), and coincided with high amplitude activity bilaterally in the motor cortices. When PV-INs were chemogenetically activated (ON state), peak amplitude was nonsignificantly reduced in $S1_W$ ($^{NS}P = 0.1756$, Fig. 5E), although the distribution of $S1_W$ activity shifted to lower amplitudes (Fig. S9B). However, chemogenetic activation of $S1_W$ PV-INs significantly reduced activity in ipsilateral $M1_W$ during $S1_W$ peaks (**$P = 0.0088$, Fig. 5E). ETA amplitude was not significantly different in contralateral $S1_W$ ($^{NS}P = 0.91$) or $M1_W$ ($^{NS}P = 0.069$). $S1_W$ homotopic correlation was similar between ON-OFF at all scales of activity (Fig. S9C). ON-OFF motor homotopic FC was reduced and straddled significance at all scales of activity, suggesting that correlation changes were not driven solely by high amplitude bursts in $S1_W$. Likewise, sensorimotor FC remained significantly weaker even after removing the top 50% high amplitude bursts, indicating that correlation strength was altered during both high and low amplitude activity in $S1_W$.

PV-INs Modulate S1 $_W$ Excitability to Ascending Contralateral Sensory Inputs, but not Ipsilateral Inputs

To assess how local changes in E/I balance affect cortical responses to ascending thalamocortical sensory input, we recorded GCaMP activity in awake mice during unilateral stimulation of their mystacial whiskers using computer-

triggered air-puffs (Fig. 6). Stimulation was presented in 20-s blocks (5 s rest, 5 air-puffs at 1 Hz, 10 s rest). To assess the pharmacokinetics of CNO, right whisker stimulation was performed at baseline, 10 min, 30 min, 1 h, 2 h, 4 h, and 12 h after CNO injection. Left whisker stimulation was collected in a separate session at baseline and 30 min after CNO injection. OFF refers to the baseline condition before CNO; ON refers to the time point 30 min after injection for both groups. Cortical dynamics were averaged to produce maps of peak evoked response (Fig. 6A) as well as histograms of peak response magnitude within left and right $S1_W$ ROIs (Fig. 6C,E). Differences in response magnitude within and between groups were compared by two-way ANOVA with Tukey's multiple comparison test (↑PV $n = 6$, ↓PV $n = 6$, Control $n = 5$). Differences within group over time (6D) were compared by two-way ANOVA with Dunnett's multiple comparison test.

Right whisker stimulation elicited responses primarily in left $S1_W$, and to a lesser extent, left $M1_W$ and the right cortex. OFF-state evoked responses in left $S1_W$ were similar between all groups ($^{NS}P > 0.99$ for all comparisons). In the ON state, evoked responses were unchanged in ↑PV (left $^{NS}P = 0.28$, right $^{NS}P = 0.71$) and Control mice (left $^{NS}P = 0.98$, right $^{NS}P > 0.99$). ↓PV mice exhibited ON-OFF differences only in left $S1_W$ (left $^{****}P < 0.0001$, right $^{NS}P > 0.99$), which peaked between 30–60 min and returned to baseline levels by 4 h after injection. Interestingly, ↓PV mice did not exhibit increased activity in ipsilateral $M1_W$ during whisker stimulation (data not shown, $^{NS}P = 0.49$), though they did during the resting state (Fig. 5B,C). Evoked responses to left whisker stimulation were primarily found in right $S1_W$, and were unchanged between the OFF and ON states for all three groups in both left and right $S1_W$.

Discussion

We investigated whether focal perturbation of inhibition/excitability can causally disrupt large-scale cortical network dynamics. To this end, we delivered AAV8 viral DREADD constructs to the left whisker barrel somatosensory cortex ($S1_W$) in three groups of clonal *PV-Cre;Thy1-GCaMP6f* mice. With this approach, we achieved spatial, temporal, and cell-type specific control over parvalbumin inhibitory interneurons in $S1_W$, while also enabling wide-field optical imaging of pyramidal neuron calcium dynamics. Our principal observations may be summarized as follows: (1) Focal chemogenetic manipulation of PV-INs induced both local changes in activity patterns and excitability as well as remote effects along intra- and interhemispheric connections; (2) Disturbances in activity in somatosensory and motor cortices differed in their tendency to spread interhemispherically; (3) FC networks exhibited plasticity in response to chronic expression of hM3Dq (↑PV) chemogenetic constructs in PV-INs. To the best of our knowledge, this represents the first study to mechanistically examine how focal changes in inhibition causally influence brain-wide network dynamics and FC. These results offer important insights that build on prior work described below.

Local Spread of E/I Imbalance

GABAergic interneurons are known to regulate local E/I balance, maintaining brain dynamics in a metastable equilibrium in which inhibition rapidly scales to counterbalance fluctuating excitatory activity (Moore et al. 2018). Optogenetic inhibition of PV-INs has been shown to disrupt E/I balance, leading to hyperexcitability, prolonged cortical up-states, and increased amplitude and spatial spread of stimulus-evoked activity (Yang et al. 2017). It has been suggested that this highly synchronized activity resembles a mild focal seizure (Chen et al. 2017), similar to the paroxysmal hyperexcitability we observed in $S1_W$ (Fig. 2). These effects exhibit surprising lateral spread: the medial-lateral diameter of $S1_W$ power changes (3.1 mm, depicted in Fig. 3A) was nearly twice as wide as the average cross-sectional area expressing DREADDs on histology (Fig. 1B), extending into adjacent regions of S1 without DREADD expression. Although dimensional comparisons between *in vivo* neuroimaging and fixed-tissue histology are challenging, this observation is corroborated by a prior report that focal activation of PV-INs in a 200-μm area affects activity in pyramidal neurons 2 mm away (Zucca et al. 2017). Similarly, a recent report has shown that a focal seizure in a 2–3-mm region can cause hemisphere-wide changes in PV-IN activity, and that pharmacologic $GABA_A$ receptor blockade can contiguously widen the seizure focus or extend it remotely to secondary foci (Liou et al. 2018). In addition, local seizures in V1 have been shown to propagate to distal portions of V1 that share the same retinotopic preference (Rossi et al. 2017). Contiguous spread of E/I disturbances may be mediated by dense connectivity of PV-INs with nearby pyramidal neurons, as well as spatial buffering between PV-INs that are laterally coupled by gap junctions. While these properties may explain why activity changes spread locally, different neural circuits may convey long distance propagation beyond the immediate reach of local inhibition.

Structural Circuits Underlying Remote Spread of Activity

We have previously reported that optogenetic stimulation of excitatory neurons elicits effective connectivity along whisker sensorimotor connections as well as homotopic spread between motor cortices, but weak homotopic spread between whisker sensory cortices, in line with cortical structural connectivity (Bauer et al. 2018). Here, we extend those findings by demonstrating that disrupting inhibitory circuits can elicit similar patterns of activity spread, but in the context of intrinsic resting state dynamics, rather than being externally driven (as with optogenetics). Thus, the effective connectivity rules we have previously reported may govern how local E/I disturbances spread through brain networks, both in experimental and clinical settings.

In particular, the present investigation reveals that E/I imbalance in $S1_W$ can spread remotely along intrahemispheric sensorimotor connections (Fig. 3 and S4). Underlying structural connectivity appears to be a key determinant of this path of spread. Tracers injected into $S1_W$ reveal strong monosynaptic projections to ipsilateral $M1_W$, compared to a low density of callosal projections terminating in contralateral $S1_W$ (Ferezou et al. 2007). Accordingly, whisker stimulation in $S1_W$ propagates forward to strongly activate $M1_W$, followed by weaker, longer-latency activation of the contralateral hemisphere (Ferezou et al. 2007). Intrahemispheric connectivity between $S1_W$ and $M1_W$ is highly reciprocal (Mao et al. 2011; Bauer et al. 2018). This direct corticocortical circuit mediates movement initiation, such that optogenetic stimulation/inhibition of $S1_W$ directly actives/inactivates $M1_W$ to increase/decrease whisking (Sreenivasan et al. 2016). Some prior evidence suggests that PV-INs in $S1_W$ gate this connection. $S1_W$ PV-INs reduce their firing rates during whisking (Pala and Petersen 2018), and optogenetic

suppression of PV-INs enhances performance on a whisker sensorimotor transformation task (Sachidhanandam et al. 2016). We find that, indeed, bidirectional manipulation of PV-INs in $S1_W$ is sufficient to modulate ipsilateral $M1_W$ activity in the resting state. Curiously, in the setting of whisker stimulation, ipsilateral $M1_W$ did not exhibit significant changes in activity in ↓PV-ON mice (Fig. 6) as it did during the resting state (Fig. 5B,C), indicating that ascending thalamocortical inputs to $S1_W$ may modulate how local E/I balance is routed intracortically. It has previously been shown that while whisker sensorimotor dynamics can function independently of the thalamus (Zagha et al. 2013), they are subject to thalamic modulation. Thalamocortical inputs to $S1_W$ form stronger synaptic connections with inhibitory interneurons than excitatory neurons, positioning the cortical interneuron population to titrate local excitability via fast feedforward inhibition (Cruikshank et al. 2007). In addition, higher order thalamic inputs have been shown to play a key role in regulating $S1_W$ interneuron dynamics and local synaptic plasticity (Williams and Holtmaat 2019). In the context of our own data, these reports would indicate that whisker stimulation may enhance thalamocortically driven feed-forward inhibition and mitigate the effects of disinhibition of sensorimotor connectivity seen in the resting state. Thus the spread of local E/I balance is likely simultaneously modulated by both local interneurons as well as ascending thalamocortical inputs.

In addition, our results demonstrate that focal cortical E/I imbalance can disrupt interhemispheric synchrony. Chronic expression of ↑PV DREADDs in left $S1_W$ caused baseline reduction of interhemispheric correlation in S1, while strengthening interhemispheric correlation in M1, effects that were reversed after activating ↑PV DREADDs in left $S1_W$ (Fig. 4). Interestingly, inhibiting left PV-INs in $S1_W$ (↓PV-ON) caused intrahemispheric hyperexcitability in left $S1_W$ and $M1_W$ (Fig. 5B,C), but these activity changes did not propagate interhemispherically; rather, homotopic synchrony for both $S1_W$ and $M1_W$ became weaker (Fig. 4). Why did interhemispheric connections relay activity changes in ↑PV mice but not ↓PV mice? One possibility is that these connections might acutely buffer against interhemispheric spread of hyperexcitability (i.e., ↓PV-ON), potentially as an endogenous protective mechanism against generalization of seizures. The notion of a ceiling on interhemispheric transmission of activity changes is in line with the recent discovery that unilateral whisker sensory deprivation potentiates transcallosal projections from the intact cortex to layer V neurons in the deprived cortex (a central hub for intracortical and subcortical connectivity), such that these synapses are maximally potentiated and LTP is occluded (Petrus et al. 2019). Furthermore, we found that dramatic ON-OFF changes in stimulation-evoked excitability remained confined within the disinhibited hemisphere, with minimal interhemispheric spread of hyperexcitability (Fig. 6). Conversely, 8 weeks of progressive E/I disturbance (↑PV-OFF) may engage homeostatic plasticity mechanisms that allow activity changes to spread interhemispherically (Fig. S8). It is noteworthy that activity changes spread interhemispherically between $M1_W$ cortices, but not $S1_W$ (Fig. 4). This points to the importance of regional variation in structural connectivity that might impact how activity changes propagate through networks. In humans, it has previously been shown that therapeutic callosotomy in epilepsy patients eliminates most interhemispheric correlation, with a notable exception: homotopic somatomotor FC is partially preserved (Johnston et al. 2008; Roland et al. 2017). Thus, interhemispheric synchrony is mediated by distinct subcortical connections depending on region, and these circuits may differentially shunt local activity changes.

Intriguingly, a recent study revealed the existence of transcallosally projecting PV-INs in M1, A1 and V1 (Rock et al. 2017). It has been proposed that long-range inhibitory connections mediate interhemispheric synchrony (Buzsáki and Wang 2012), and histological evidence seems to indicate that transcallosal PV-INs are a general feature of the cortex (Rock et al. 2017). However, transcallosal PV-INs have not yet been reported in S1 to our knowledge; after careful review, we could not detect any mCherry-labeled intracortical projections in the corpus callosum or the contralateral hemisphere in any of our mice. Future studies may determine the specific cellular conduits of interhemispheric spread of activity changes, and how they vary regionally.

Disambiguating Changes in Functional Connectivity

Using ETA effective connectivity analysis, we are able to show that changes in correlation (FC) are largely driven by high amplitude bursts of hyperexcitability. We show that bursts lead to enhanced correlation when they propagate between nodes of a network (e.g., intrahemispheric sensorimotor FC), and weakened correlation when they do not transmit between nodes (e.g., $S1_W$ homotopic FC), and that differences in correlation largely return to nonsignificant levels after bursts are removed from time series (Fig. S9). These findings carry important implications for interpreting pathological hypo- and hyperconnectivity in BOLD fMRI data. The effects we observed in delta band GCaMP FC (Fig. 4) are also present in infraslow hemodynamics (Figs S6 and S7), despite the fact that bursting dynamics are not present in the oxy-hemoglobin signal (Fig. S3). This result indicates that BOLD fMRI may capture FC changes induced by paroxysmal hyperactivity in neural dynamics, even though the associated activity change is not represented in BOLD dynamics, which are relatively slow.

In addition, it is possible that correlation differences are also driven by disruptions in gamma oscillations. PV-INs are pacemakers that drive high frequency gamma activity (Cardin et al. 2009; Sohal et al. 2009; Chen et al. 2017). These fast oscillations have been observed to modulate slower activity, and may interact with low frequency oscillations in a manner that supports efficient long-range temporal coordination (Buzsáki and Wang 2012; Uhlhaas and Singer 2012). In support of this hypothesis, slow fluctuations (<0.1 Hz) in gamma LFP power exhibit long-range synchrony (Nir et al. 2008), which exhibits a similar correlation structure to infraslow BOLD FC networks (He et al. 2008).

In our own data, chemogenetic inhibition of PV-INs manifested in broadband increases in LFP power (S2), consistent with a prior report (Nguyen et al. 2014), though only increases in < 25 Hz activity were statistically significant in our data. This stands in contrast to a seminal investigation by Sohal et al., who optogenetically inhibited PV-INs and observed significantly reduced 30–80 Hz gamma power but increased 10–30 Hz oscillations (Sohal et al. 2009). These opposite effects in the gamma band may be due to our use of DREADDs (GPCR-based signaling, tonic change in membrane excitability) versus optogenetic inhibition (ionotropic signaling, phasic patterned firing). Another possibility, elegantly demonstrated with optogenetics by Moore et al., is that inhibition of PV-INs can paradoxically increase gamma band activity in downstream PV-INs as they counterbalance increased excitatory activity (Moore et al. 2018). In contrast, we found that activation of local PV-INs with hM3Dq

DREADDs did not significantly alter local $S1_W$ activity (even while activity significantly decreased remotely in $M1_W$), which may reflect the limited sensitivity of our recording techniques or the inherent capacity of $S1_W$ ensemble dynamics to buffer against increased PV-IN inhibition. In addition, the relatively weak effect of hM3Dq DREADDs versus the strong effect of hM4Di DREADDs may reflect differences between excitatory Gq signaling (hM3Dq) via the IP3/DAG pathway versus inhibitory Gi signaling (hM4Di) through cAMP-dependent pathways, which may not produce symmetrical effects on PV-IN activity. Further investigation with single unit recordings and slice electrophysiology may better define contributions of PV-IN activity to FC changes.

Plasticity in FC Induced by Chemogenetic Constructs in CNO-Naïve Mice

Notably, propagation of local E/I balance induced changes remotely along sensorimotor connections. We found that $M1_W$ excitability (Fig. 3 and S4) and sensorimotor synchrony (Fig. 4) were consistently elevated in ↑PV-OFF mice at baseline. These differences developed progressively with 8 weeks of hM3Dq expression in CNO-naïve mice (Fig. S8). Importantly, these baseline changes are *opposite* of the acute effects of activating hM3Dq, which dampened $M1_W$ excitability (Fig. 3) and sensorimotor synchrony (Fig. 4). In light of these findings, we hypothesize that hM3Dq DREADDs exhibit leak signaling, and that chronic low-level activation of PV-INs in $S1_W$ induces compensatory plasticity that disinhibits sensorimotor connectivity and causes sustained hyperexcitability in $M1_W$. These findings have important implications for the study of neural circuits *in vivo*. First, our study demonstrates that DREADDs, a tool that has exploded in popularity in recent years, can perturb brain activity in the absence of activating ligand, CNO. Second, our data suggest that local chemo- and optogenetic manipulations commonly used in local neural recordings can produce long-range effects on brain activity outside the manipulated area, which may in turn disrupt inputs feeding back in on local activity.

How might chronic leak in hM3Dq DREADDs lead to compensatory baseline changes that are opposite to the effects of acute hM3Dq activation? One such mechanism may be paradoxical inhibition of PV-INs downstream of leak-activated PV-INs, the reverse of the effect reported by Moore et al. 2018. In addition, leaky chemogenetic activation of PV-INs might dysregulate the NRG1/ErbB4 axis, which positively regulates the strength of excitatory synaptic inputs onto PV-INs that drive feed-forward inhibition, and exhibits compensatory plasticity in response to chemogenetic manipulation (Sun et al. 2016). Lastly, chemogenetic activation of PV-INs may alter their myelination and axonal morphology in a manner that impacts connectivity (Stedehouder et al. 2018). Further investigation of the effects of chemogenetic constructs on cortical networks is ongoing in our laboratory.

Methodologic Limitations

This study is limited in its ability to define a specific role for PV-INs in influencing network dynamics, primarily because PV-INs are exceedingly heterogeneous in their connectivity within neural circuits. Within $S1_W$, it has been shown that different groups of PV-INs are linked by gap-junctions to form distinct components of a patterned inhibitory scaffold around cortical whisker barrel circuits (Shigematsu et al. 2018). Thus different classes of PV-expressing neurons may differently contribute to brain dynamics (locally and globally), which will require further investigation as techniques are developed for differentiating subtypes in neural recordings. In addition, PV-INs work in concert with other GABAergic subtypes (e.g., somatostatin, VIP), whose contributions to network dynamics warrant additional investigation.

Implications for Translation to Neurologic Injury

Focal E/I imbalance may be a therapeutic target for rectifying widespread brain network dysfunction after focal neurologic injury. In addition, the present findings may provide mechanistic context for understanding FC patterns as a tool to localize injury, predict and track recovery outcomes, and identify potential therapeutic interventions. For example, traumatic brain injury (TBI) leads to progressive failure of inhibitory circuits, associated with loss of PV immunoreactivity and dissolution of perineuronal nets supporting PV-INs (Hsieh et al. 2017). Our findings suggest that such a loss of inhibition may explain hyperconnectivity in brain FC networks after TBI (Caeyenberghs et al. 2017). Likewise, many mechanistic studies have specifically implicated local PV-IN dysfunction in seizure onset (Jiang et al. 2016), which our results suggest may mediate anomalous functional connectivity between epileptogenic zones and the rest of the brain (Centeno and Carmichael 2014; Englot et al. 2016; Xiao et al. 2017; Farrell et al. 2019). Furthermore, animal and human studies of stroke have shown that excess inhibition hampers large-scale brain networks and functional recovery after ischemia, and that therapies targeting inhibitory circuits improve network synchrony and functional recovery (Liepert et al. 2000; Clarkson et al. 2010; Zeiler et al. 2013; Kim et al. 2014; Blicher et al. 2015; Alia et al. 2016; Quattromani et al. 2018). Thus, specific molecular and cellular processes underlying imbalance in excitability may serve as potential therapeutic targets for restoring large-scale brain network connectivity after injury.

Supplementary Material

Supplementary material is available at *Cerebral Cortex* online.

Author Contributions

Experimental Design: Z.P.R., A.W.K., J.M.L.
Data Acquisition: Z.P.R., D.K.
Data Analysis: Z.P.R., R.V.R.
Technical Resources (Neuroimaging): J.C., A.Q.B.
Technical Resources (Electrophysiology): M.E.R., B.A., A.M., A.Q.B.
Histology: P.Y., Z.P.R., D.K., L.C.
Project Supervision: J.M.L., M.E.R., J.P.C., A.Q.B., A.Z.S, L.H.S.
Graduate Student Mentorship: J.M.L. (Z.P.R., A.W.K., L.C.), M.E.R. (R.V.R., A.M.), L.H.S. (B.A.)
Writing—Original Draft: Z.P.R., R.V.R., A.Z.S., J.M.L.
Writing—Review & Approval: Z.P.R., R.V.R., P.Y., D.K., A.W.K., L.C., B.A., A.M., L.H.S., A.Q.B., A.Z.S., J.P.C., M.E.R, J.M.L.

Funding

National Institute of Health (grant F31NS103275 to Z.P.R.; F31NS089135 to A.W.K.; F30MH106253 to A.M.; F31NS098791 to L.C.; R01NS084028, R01NS085419 and R01NS094692 to J.M.L.;

R01NS099429, R01NS078223 to J.P.C.; P01NS080675 to M.E.R.; P30NS098577 to A.Z.S.; R01NS102870, K25NS083754 to A.Q.B.; R01MH102471 and R21NS105090 to L.H.S.; NSF grant DGE-1745038 to R.V.R. and the McDonnell Center for Systems Neuroscience).

Notes

We thank the Hope Center Animal Surgery Core, in particular Karen Smith and Ronald Perez, for their assistance with mouse husbandry and surgeries for these experiments, the Washington University Instrument Machine Shop for fabricating cranial windows and adaptors for experiments, and the Hope Center Viral Vectors Core for producing chemogenetic viral constructs. Mouse illustration in Figure 1A was provided by Anushree Seth in association with InPrint at Washington University in St. Louis. *Conflict of Interest*: The authors declare no competing interests.

References

Alia C, Spalletti C, Lai S, Panarese A, Micera S, Caleo M. 2016. Reducing Gabaa-mediated inhibition improves forelimb motor function after focal cortical stroke in mice. *Sci Rep*. 6:37823.

Barral J, Reyes AD. 2016. Synaptic scaling rule preserves excitatory-inhibitory balance and salient neuronal network dynamics. *Nat Neurosci*. 19(12):1690–1696.

Bauer AQ, Kraft AW, Baxter GA, Wright PW, Reisman MD, Bice AR, Park JJ, Bruchas MR, Snyder AZ, Lee JM, et al. 2018. Effective connectivity measured using optogenetically evoked hemodynamic signals exhibits topography distinct from resting state functional connectivity in the mouse. *Cereb Cortex*. 28(1):370–386.

Bhatia A, Moza S, Bhalla US. 2019. Precise excitation-inhibition balance controls gain and timing in the hippocampus. *Elife* 8:1–29.

Blicher JU, Near J, Naess-Schmidt E, Stagg CJ, Johansen-Berg H, Nielsen JF, Ostergaard L, Ho YC. 2015. Gaba levels are decreased after stroke and gaba changes during rehabilitation correlate with motor improvement. *Neurorehabil Neural Repair*. 29(3):278–286.

Buzsáki G, Wang XJ. 2012. Mechanisms of gamma oscillations. *Annu Rev Neurosci*. 35:203–225.

Caeyenberghs K, Verhelst H, Clemente A, Wilson PH. 2017. Mapping the functional connectome in traumatic brain injury: what can graph metrics tell us? *Neuroimage*. 160:113–123.

Calin A, Stancu M, Zagrean AM, Jefferys JGR, Ilie AS, Akerman CJ. 2018. Chemogenetic recruitment of specific interneurons suppresses seizure activity. *Front Cell Neurosci*. 12:293.

Cardin JA, Carlen M, Meletis K, Knoblich U, Zhang F, Deisseroth K, Tsai LH, Moore CI. 2009. Driving fast-spiking cells induces gamma rhythm and controls sensory responses. *Nature*. 459(7247):663–667.

Carmichael ST. 2012. Brain excitability in stroke: the yin and yang of stroke progression. *Arch Neurol*. 69(2):161–167.

Centeno M, Carmichael DW. 2014. Network connectivity in epilepsy: resting state fmri and eeg-fmri contributions. *Front Neurol*. 5:93.

Chandrasekar A, Olde Heuvel F, Tar L, Hagenston AM, Palmer A, Linkus B, Ludolph AC, Huber-Lang M, Boeckers T, Bading H, et al. 2018. Parvalbumin interneurons shape neuronal vulnerability in blunt tbi. *Cereb Cortex*. 29, 2701–2715.

Chen G, Zhang Y, Li X, Zhao X, Ye Q, Lin Y, Tao HW, Rasch MJ, Zhang X. 2017. Distinct inhibitory circuits orchestrate cortical beta and gamma band oscillations. *Neuron*. 96(6):1403, e1406–1403, e1418.

Clarkson AN, Huang BS, Macisaac SE, Mody I, Carmichael ST. 2010. Reducing excessive gaba-mediated tonic inhibition promotes functional recovery after stroke. *Nature*. 468(7321):305–309.

Cruikshank SJ, Lewis TJ, Connors BW. 2007. Synaptic basis for intense thalamocortical activation of feedforward inhibitory cells in neocortex. *Nat Neurosci*. 10(4):462–468.

Deco G, Ponce-Alvarez A, Hagmann P, Romani GL, Mantini D, Corbetta M. 2014. How local excitation-inhibition ratio impacts the whole brain dynamics. *J Neurosci*. 34(23):7886–7898.

Duff EP, Makin T, Cottaar M, Smith SM, Woolrich MW. 2018. Disambiguating brain functional connectivity. *Neuroimage*. 173:540–550.

Englot DJ, Konrad PE, Morgan VL. 2016. Regional and global connectivity disturbances in focal epilepsy, related neurocognitive sequelae, and potential mechanistic underpinnings. *Epilepsia*. 57(10):1546–1557.

Farrell JS, Nguyen Q-A, Soltesz I. 2019. Resolving the micro-macro disconnect to address core features of seizure networks. *Neuron*. 101(6):1016–1028.

Ferezou I, Haiss F, Gentet LJ, Aronoff R, Weber B, Petersen CC. 2007. Spatiotemporal dynamics of cortical sensorimotor integration in behaving mice. *Neuron*. 56(5):907–923.

Fox MD, Raichle ME. 2007. Spontaneous fluctuations in brain activity observed with functional magnetic resonance imaging. *Nat Rev Neurosci*. 8(9):700–711.

Fox MD, Zhang D, Snyder AZ, Raichle ME. 2009. The global signal and observed anticorrelated resting state brain networks. *J Neurophysiol*. 101(6):3270–3283.

Franklin KBJ, Paxinos G. 2012. *The mouse brain in stereotactic coordinates*. New York: Academic Press.

Funk CM, Peelman K, Bellesi M, Marshall W, Cirelli C, Tononi G. 2017. Role of somatostatin-positive cortical interneurons in the generation of sleep slow waves. *J Neurosci*. 37(38):9132–9148.

He BJ, Snyder AZ, Zempel JM, Smyth MD, Raichle ME. 2008. Electrophysiological correlates of the brain's intrinsic large-scale functional architecture. *Proc Natl Acad Sci U S A*. 105(41):16039–16044.

Hensch TK. 2005. Critical period plasticity in local cortical circuits. *Nat Rev Neurosci*. 6(11):877–888.

Hsieh TH, Lee HHC, Hameed MQ, Pascual-Leone A, Hensch TK, Rotenberg A. 2017. Trajectory of parvalbumin cell impairment and loss of cortical inhibition in traumatic brain injury. *Cereb Cortex*. 27(12):5509–5524.

Jiang X, Lachance M, Rossignol E. 2016. Involvement of cortical fast-spiking parvalbumin-positive basket cells in epilepsy. *Prog Brain Res*. 226:81–126.

Johnston JM, Vaishnavi SN, Smyth MD, Zhang D, He BJ, Zempel JM, Shimony JS, Snyder AZ, Raichle ME. 2008. Loss of resting interhemispheric functional connectivity after complete section of the corpus callosum. *J Neurosci*. 28(25):6453–6458.

Kim YK, Yang EJ, Cho K, Lim JY, Paik NJ. 2014. Functional recovery after ischemic stroke is associated with reduced gabaergic inhibition in the cerebral cortex: a gaba pet study. *Neurorehabil Neural Repair*. 28(6):576–583.

Kraft AW, Bauer AQ, Culver JP, Lee JM. 2018. Sensory deprivation after focal ischemia in mice accelerates brain remapping

and improves functional recovery through arc-dependent synaptic plasticity. *Sci Transl Med*. 10(426).

Kraft AW, Mitra A, Bauer AQ, Snyder AZ, Raichle ME, Culver JP, Lee JM. 2017. Visual experience sculpts whole-cortex spontaneous infraslow activity patterns through an arc-dependent mechanism. *Proc Natl Acad Sci U S A*. 114(46):E9952–E9961.

Kubota Y, Kamatani D, Tsukano H, Ohshima S, Takahashi K, Hishida R, Kudoh M, Takahashi S, Shibuki K. 2008. Transcranial photo-inactivation of neural activities in the mouse auditory cortex. *Neurosci Res*. 60(4):422–430.

Kuhlman SJ, Olivas ND, Tring E, Ikrar T, Xu X, Trachtenberg JT. 2013. A disinhibitory microcircuit initiates critical-period plasticity in the visual cortex. *Nature*. 501(7468):543–546.

Liepert J, Storch P, Fritsch A, Weiller C. 2000. Motor cortex disinhibition in acute stroke. *Clin Neurophysiol*. 111(4):671–676.

Liou JY, Ma H, Wenzel M, Zhao M, Baird-Daniel E, Smith EH, Daniel A, Emerson R, Yuste R, Schwartz TH, et al. 2018. Role of inhibitory control in modulating focal seizure spread. *Brain*. 141(7):2083–2097.

Liu J, Zhang MQ, Wu X, Lazarus M, Cherasse Y, Yuan MY, Huang ZL, Li RX. 2017. Activation of parvalbumin neurons in the rostro-dorsal sector of the thalamic reticular nucleus promotes sensitivity to pain in mice. *Neuroscience*. 366:113–123.

Ma Y, Shaik MA, Kozberg MG, Kim SH, Portes JP, Timerman D, Hillman EM. 2016. Resting-state hemodynamics are spatiotemporally coupled to synchronized and symmetric neural activity in excitatory neurons. *Proc Natl Acad Sci U S A*. 113(52):E8463–E8471.

Maffei A, Nataraj K, Nelson SB, Turrigiano GG. 2006. Potentiation of cortical inhibition by visual deprivation. *Nature*. 443(7107):81–84.

Mao T, Kusefoglu D, Hooks BM, Huber D, Petreanu L, Svoboda K. 2011. Long-range neuronal circuits underlying the interaction between sensory and motor cortex. *Neuron*. 72(1):111–123.

Mishra AM, Bai X, Sanganahalli BG, Waxman SG, Shatillo O, Grohn O, Hyder F, Pitkanen A, Blumenfeld H. 2014. Decreased resting functional connectivity after traumatic brain injury in the rat. *PLoS One*. 9(4):e95280.

Mitra A, Kraft A, Wright P, Acland B, Snyder AZ, Rosenthal Z, Czerniewski L, Bauer A, Snyder L, Culver J, et al. 2018. Spontaneous infra-slow brain activity has unique spatiotemporal dynamics and laminar structure. *Neuron*. 98(2):297–305 e296.

Moore AK, Weible AP, Balmer TS, Trussell LO, Wehr M. 2018. Rapid rebalancing of excitation and inhibition by cortical circuitry. *Neuron*. 97(6):1341–1355 e1346.

Murphy MC, Chan KC, Kim SG, Vazquez AL. 2018. Macroscale variation in resting-state neuronal activity and connectivity assessed by simultaneous calcium imaging, hemodynamic imaging and electrophysiology. *Neuroimage*. 169:352–362.

Nguyen R, Morrissey MD, Mahadevan V, Cajanding JD, Woodin MA, Yeomans JS, Takehara-Nishiuchi K, Kim JC. 2014. Parvalbumin and gad65 interneuron inhibition in the ventral hippocampus induces distinct behavioral deficits relevant to schizophrenia. *J Neurosci*. 34(45):14948–14960.

Nir Y, Mukamel R, Dinstein I, Privman E, Harel M, Fisch L, Gelbard-Sagiv H, Kipervasser S, Andelman F, Neufeld MY, et al. 2008. Interhemispheric correlations of slow spontaneous neuronal fluctuations revealed in human sensory cortex. *Nat Neurosci*. 11(9):1100–1108.

Pala A, Petersen CC. 2018. State-dependent cell-type-specific membrane potential dynamics and unitary synaptic inputs in awake mice. *Elife*. 7:1–13.

Petrus E, Saar G, Ma Z, Dodd S, Isaac JTR, Koretsky AP. 2019. Interhemispheric plasticity is mediated by maximal potentiation of callosal inputs. *Proc Natl Acad Sci U S A*.

Quattromani MJ, Hakon J, Rauch U, Bauer AQ, Wieloch T. 2018. Changes in resting-state functional connectivity after stroke in a mouse brain lacking extracellular matrix components. *Neurobiol Dis*. 112:91–105.

Rock C, Zurita H, Lebby S, Wilson CJ, Apicella AJ. 2017. Cortical circuits of callosal gabaergic neurons. *Cereb Cortex*. 1–14.

Roland JL, Snyder AZ, Hacker CD, Mitra A, Shimony JS, Limbrick DD, Raichle ME, Smyth MD, Leuthardt EC. 2017. On the role of the corpus callosum in interhemispheric functional connectivity in humans. *Proc Natl Acad Sci U S A*. 114(50): 13278–13283.

Rossi LF, Wykes RC, Kullmann DM, Carandini M. 2017. Focal cortical seizures start as standing waves and propagate respecting homotopic connectivity. *Nat Commun*. 8(1):217.

Roth BL. 2016. Dreadds for neuroscientists. *Neuron*. 89(4):683–694.

Sachidhanandam S, Sermet BS, Petersen CCH. 2016. Parvalbumin-expressing gabaergic neurons in mouse barrel cortex contribute to gating a goal-directed sensorimotor transformation. *Cell Rep*. 15(4):700–706.

Shigematsu N, Nishi A, Fukuda T. 2018. Gap junctions interconnect different subtypes of parvalbumin-positive interneurons in barrels and septa with connectivity unique to each subtype. *Cereb Cortex*. 29:1414–1429.

Silasi G, Murphy TH. 2014. Stroke and the connectome: how connectivity guides therapeutic intervention. *Neuron*. 83(6):1354–1368.

Silasi G, Xiao D, Vanni MP, Chen AC, Murphy TH. 2016. Intact skull chronic windows for mesoscopic wide-field imaging in awake mice. *J Neurosci Methods*. 267:141–149.

Sohal VS, Zhang F, Yizhar O, Deisseroth K. 2009. Parvalbumin neurons and gamma rhythms enhance cortical circuit performance. *Nature*. 459(7247):698–702.

Sreenivasan V, Esmaeili V, Kiritani T, Galan K, Crochet S, Petersen CCH. 2016. Movement initiation signals in mouse whisker motor cortex. *Neuron*. 92(6):1368–1382.

Stedehouder J, Brizee D, Shpak G, Kushner SA. 2018. Activity-dependent myelination of parvalbumin interneurons mediated by axonal morphological plasticity. *J Neurosci*. 38(15):3631–3642.

Sun Y, Ikrar T, Davis MF, Gong N, Zheng X, Luo ZD, Lai C, Mei L, Holmes TC, Gandhi SP, et al. 2016. Neuregulin-1/erbb4 signaling regulates visual cortical plasticity. *Neuron*. 92(1): 160–173.

Uhlhaas PJ, Singer W. 2012. Neuronal dynamics and neuropsychiatric disorders: toward a translational paradigm for dysfunctional large-scale networks. *Neuron*. 75(6):963–980.

Vazquez AL, Fukuda M, Crowley JC, Kim SG. 2014. Neural and hemodynamic responses elicited by forelimb- and photo-stimulation in channelrhodopsin-2 mice: insights into the hemodynamic point spread function. *Cereb Cortex*. 24(11):2908–2919.

White BR, Bauer AQ, Snyder AZ, Schlaggar BL, Lee JM, Culver JP. 2011. Imaging of functional connectivity in the mouse brain. *PLoS One*. 6(1):e16322.

Williams LE, Holtmaat A. 2019. Higher-order thalamocortical inputs gate synaptic long-term potentiation via disinhibition. *Neuron*. 101(1):91, e104–91, e102.

Wright PW, Brier LM, Bauer AQ, Baxter GA, Kraft AW, Reisman MD, Bice AR, Snyder AZ, Lee JM, Culver JP. 2017. Functional connectivity structure of cortical calcium dynam-

ics in anesthetized and awake mice. *PLoS One*. 12(10): e0185759.

Xiao F, An D, Zhou D. 2017. Functional mri-based connectivity analysis: a promising tool for the investigation of the pathophysiology and comorbidity of epilepsy. *Seizure*. 44: 37–41.

Yang JW, Prouvot PH, Reyes-Puerta V, Stuttgen MC, Stroh A, Luhmann HJ. 2017. Optogenetic modulation of a minor fraction of parvalbumin-positive interneurons specifically affects spatiotemporal dynamics of spontaneous and sensory-evoked activity in mouse somatosensory cortex in vivo. *Cereb Cortex*. 27(12):5784–5803.

Yizhar O, Fenno LE, Prigge M, Schneider F, Davidson TJ, O'Shea DJ, Sohal VS, Goshen I, Finkelstein J, Paz JT, et al. 2011. Neocortical excitation/inhibition balance in information processing and social dysfunction. *Nature*. 477(7363):171–178.

Zagha E, Casale AE, Sachdev RN, McGinley MJ, McCormick DA. 2013. Motor cortex feedback influences sensory processing by modulating network state. *Neuron*. 79(3): 567–578.

Zeiler SR, Gibson EM, Hoesch RE, Li MY, Worley PF, O'Brien RJ, Krakauer JW. 2013. Medial premotor cortex shows a reduction in inhibitory markers and mediates recovery in a mouse model of focal stroke. *Stroke*. 44(2):483–489.

Zucca S, D'Urso G, Pasquale V, Vecchia D, Pica G, Bovetti S, Moretti C, Varani S, Molano-Mazon M, Chiappalone M, et al. 2017. An inhibitory gate for state transition in cortex. *Elife*. 6:1–31.